Single π^+ Electroproduction on the Proton in the First and Second Resonance Regions at $0.25\ \mathbf{GeV}^2 < Q^2 < 0.65\ \mathbf{GeV}^2$ Using CLAS

H. Egiyan,[1,2] I.G. Aznauryan,[4] V.D. Burkert,[1] K.A. Griffioen,[2] K. Joo,[11,1] R. Minehart,[3] L.C. Smith,[3] G. Adams,[34] P. Ambrozewicz,[14] E. Anciant,[6] M. Anghinolfi,[19] B. Asavapibhop,[26] G. Audit,[6] T. Auger,[6] H. Avakian,[1,18] H. Bagdasaryan,[31] J.P. Ball,[5] N. Baltzel,[37] S. Barrow,[15] M. Battaglieri,[19] K. Beard,[23] M. Bektasoglu,[30,*] M. Bellis,[34] N. Benmouna,[16] N. Bianchi,[18] A.S. Biselli,[34,8] S. Boiarinov,[1] B.E. Bonner,[35] S. Bouchigny,[20] R. Bradford,[8] D. Branford,[13] W.J. Briscoe,[16] W.K. Brooks,[1] C. Butuceanu,[2] J.R. Calarco,[28] S.L. Careccia,[31] D.S. Carman,[30] B. Carnahan,[9] C. Cetina,[16] S. Chen,[15] P.L. Cole,[38] A. Coleman,[2] D. Cords,[1] P. Corvisiero,[19] D. Crabb,[3] H. Crannell,[9] J.P. Cummings,[34] E. DeSanctis,[18] R. DeVita,[19] P.V. Degtyarenko,[1] H. Denizli,[32] L. Dennis,[15] K.V. Dharmawardane,[31] C. Djalali,[37] G.E. Dodge,[31] J. Donnely,[17] D. Doughty,[10,1] P. Dragovitsch,[15] M. Dugger,[5] S. Dytman,[32] O.P. Dzyubak,[37] M. Eckhause,[2] K.S. Egiyan,[4] L. Elouadrhiri,[1] A. Empl,[34] P. Eugenio,[15] R. Fatemi,[3] G. Fedotov,[27] G. Feldman,[16] R.J. Feuerbach,[8] T.A. Forest,[31] H. Funsten,[2] S.J. Gaff,[12] M. Gai,[11] G. Gavalian,[31] S. Gilad,[25] G.P. Gilfoyle,[36] K.L. Giovanetti,[23] P. Girard,[37] G.T. Goetz,[7] C.I.O. Gordon,[17] R. Gothe,[37] M. Guidal,[20] M. Guillo,[37] N. Guler,[31] L. Guo,[1] V. Gyurjyan,[1] C. Hadjidakis,[20] R.S. Hakobyan,[9] J. Hardie,[10,1] D. Heddle,[10,1] F.W. Hersman,[28] K. Hicks,[30] R.S. Hicks,[26] I. Hleiqawi,[30] M. Holtrop,[28] J. Hu,[34] C.E. Hyde-Wright,[31] Y. Ilieva,[16] D.G. Ireland,[17] B. Ishkhanov,[27] M.M. Ito,[1] D. Jenkins,[40] H.G. Juengst,[16] J.H. Kelley,[12] J.D. Kellie,[17] M. Khandaker,[29] D.H. Kim,[24] K.Y. Kim,[32] K. Kim,[24] M.S. Kim,[24] W. Kim,[24] A. Klein,[31] F.J. Klein,[1,9] A..V. Klimenko,[31] M. Klusman,[34] M. Kossov,[22] L.H. Kramer,[14] Y. Kuang,[2] V. Kubarovsky,[34] S.E. Kuhn,[31] J. Kuhn,[8] J. Lachniet,[8] J.M. Laget,[6,1] J. Langheinrich,[37] D. Lawrence,[26] Ji Li,[34] K. Livingston,[17] A. Longhi,[9] K. Lukashin,[1,9] J.J. Manak,[1] C. Marchand,[6] S. McAleer,[15] B. McKinnon,[17] J.W.C. McNabb,[8] B.A. Mecking,[1] S. Mehrabyan,[32] J.J. Melone,[17] M.D. Mestayer,[1] C.A. Meyer,[8] K. Mikhailov,[22] M. Mirazita,[18] R. Miskimen,[26] V. Mokeev,[27,1] L. Morand,[6] S.A. Morrow,[6,20] V. Muccifora,[18] J. Mueller,[32] L.Y. Murphy,[16] G.S. Mutchler,[35] J. Napolitano,[34] R. Nasseripour,[14] S.O. Nelson,[12] S. Niccolai,[16,20] G. Niculescu,[30] I. Niculescu,[23,16] B.B. Niczyporuk,[1] R.A. Niyazov,[1] M. Nozar,[1] G.V. O'Rielly,[16] M. Osipenko,[19] K. Park,[24] E. Pasyuk,[5] G. Peterson,[26] S.A. Philips,[16] N. Pivnyuk,[22] D. Pocanic,[3] O. Pogorelko,[22] E. Polli,[18] S. Pozdniakov,[22] B.M. Preedom,[37] J.W. Price,[7] Y. Prok,[3] D. Protopopescu,[17] L.M. Qin,[31] B.A. Raue,[14] G. Riccardi,[15] G. Ricco,[19] M. Ripani,[19] B.G. Ritchie,[5] F. Ronchetti,[18,33] G. Rosner,[17] P. Rossi,[18] D. Rowntree,[25] P.D. Rubin,[36] F. Sabatié,[6] K. Sabourov,[12] C. Salgado,[29] J.P. Santoro,[40] V. Sapunenko,[19] M. Sargsyan,[14] R.A. Schumacher,[8] V.S. Serov,[22] A. Shafi,[16] Y.G. Sharabian,[4,1] J. Shaw,[26] S. Simionatto,[16] A.V. Skabelin,[25] E.S. Smith,[1] D.I. Sober,[9] M. Spraker,[12] A. Stavinsky,[22] S. Stepanyan,[1,31] P. Stoler,[34] I.I. Strakovsky,[16] S. Strauch,[16] M. Taiuti,[19] S. Taylor,[35] D.J. Tedeschi,[37] U. Thoma,[1,21] R. Thompson,[32] A. Tkabladze,[30] L. Todor,[8] C. Tur,[37] M. Ungaro,[34] M.F. Vineyard,[39,36] A.V. Vlassov,[22] K. Wang,[3] L.B. Weinstein,[31] H. Weller,[12] D.P. Weygand,[1] C.S. Whisnant,[37,23] E. Wolin,[1] M.H. Wood,[37] A. Yegneswaran,[1] J. Yun,[31] J. Zhang,[31] J. Zhao,[25] and Z. Zhou[25]

(The CLAS Collaboration)

[1] *Thomas Jefferson National Accelerator Facility, Newport News, Virginia 23606*
[2] *College of William and Mary, Williamsburg, Virginia 23187-8795*
[3] *University of Virginia, Charlottesville, Virginia 22901*
[4] *Yerevan Physics Institute, 375036 Yerevan, Armenia*
[5] *Arizona State University, Tempe, Arizona 85287-1504*
[6] *CEA-Saclay, Service de Physique Nucléaire, F91191 Gif-sur-Yvette, France*
[7] *University of California at Los Angeles, Los Angeles, California 90095-1547*
[8] *Carnegie Mellon University, Pittsburgh, Pennsylvania 15213*
[9] *Catholic University of America, Washington, D.C. 20064*
[10] *Christopher Newport University, Newport News, Virginia 23606*
[11] *University of Connecticut, Storrs, Connecticut 06269*
[12] *Duke University, Durham, North Carolina 27708-0305*
[13] *Edinburgh University, Edinburgh EH9 3JZ, United Kingdom*
[14] *Florida International University, Miami, Florida 33199*
[15] *Florida State University, Tallahassee, Florida 32306*
[16] *The George Washington University, Washington, DC 20052*
[17] *University of Glasgow, Glasgow G12 8QQ, United Kingdom*
[18] *INFN, Laboratori Nazionali di Frascati, Frascati, Italy*
[19] *INFN, Sezione di Genova, 16146 Genova, Italy*
[20] *Institut de Physique Nucleaire ORSAY, Orsay, France*

[21] Institute für Strahlen und Kernphysik, Universität Bonn, Germany
[22] Institute of Theoretical and Experimental Physics, Moscow, 117259, Russia
[23] James Madison University, Harrisonburg, Virginia 22807
[24] Kungpook National University, Daegu 702-701, South Korea
[25] Massachusetts Institute of Technology, Cambridge, Massachusetts 02139-4307
[26] University of Massachusetts, Amherst, Massachusetts 01003
[27] Moscow State University, Skabeltsin Nuclear Physics Institute, 119899 Moscow, Russia
[28] University of New Hampshire, Durham, New Hampshire 03824-3568
[29] Norfolk State University, Norfolk, Virginia 23504
[30] Ohio University, Athens, Ohio 45701
[31] Old Dominion University, Norfolk, Virginia 23529
[32] University of Pittsburgh, Pittsburgh, Pennsylvania 15260
[33] Universita' di ROMA III, 00146 Roma, Italy
[34] Rensselaer Polytechnic Institute, Troy, New York 12180-3590
[35] Rice University, Houston, Texas 77005-1892
[36] University of Richmond, Richmond, Virginia 23173
[37] University of South Carolina, Columbia, South Carolina 29208
[38] University of Texas at El Paso, El Paso, Texas 79968
[39] Union College, Schenectady, NY 12308
[40] Virginia Polytechnic Institute and State University, Blacksburg, Virginia 24061-0435

(Dated: January 3, 2006)

The $ep \to e'\pi^+ n$ reaction was studied in the first and second nucleon resonance regions in the 0.25 GeV^2 $< Q^2 <$ 0.65 GeV^2 range using the CLAS detector at Thomas Jefferson National Accelerator Facility. For the first time the absolute cross sections were measured covering nearly the full angular range in the hadronic center-of-mass frame. The structure functions σ_{TL}, σ_{TT} and the linear combination $\sigma_T + \epsilon\sigma_L$ were extracted by fitting the ϕ-dependence of the measured cross sections, and were compared to the MAID and Sato-Lee models.

PACS numbers:

INTRODUCTION

The structure of the nucleon and its excited states has been one of the most extensively studied subjects in nuclear and particle physics for many years. It allows us to understand important aspects of the underlying theory of the strong interaction, QCD, in the confinement regime where solutions are very difficult to obtain. Elastic electron scattering experiments provide information on the ground state of the nucleon, while studying the Q^2 evolution of the transition amplitudes from the nucleon ground state into the excited states provides insight into the internal structure of the excited nucleon. Single-pion electroproduction is one of the most suitable processes for studying the transitions to states with masses below 1.7 GeV because of the large πN coupling for these states [1]. The detection of two out of three outgoing particles is sufficient to achieve a complete measurement of the differential cross sections in order to attempt the extraction of the amplitudes for the individual resonances. The kinematic quantities of the $ep \to e'\pi^+ n$ reaction is shown in Fig. 1. The virtual photon is described by the four-momentum transfer Q^2, energy transfer ν and the polarization parameter ϵ:

$$Q^2 = 4E_i E_f \sin^2\frac{\theta_e}{2}, \tag{1}$$

$$\epsilon = \left[1 + 2\left(1 + \frac{\nu^2}{Q^2}\right)\tan^2\frac{\theta_e}{2}\right]^{-1}, \tag{2}$$

$$\nu = E_i - E_f, \tag{3}$$

where E_i and E_f are the initial and final energies of the electron and θ_e is the electron scattering angle. The mass of the hadronic system is given by:

$$W = \sqrt{M^2 + 2M\nu - Q^2}, \tag{4}$$

where M is the proton mass. The two hadron production angles θ and ϕ are defined in the center-of-mass (c.m.) reference frame, with θ being the angle between the outgoing pion and the direction of the three-momentum transfer, and ϕ being the angle between the electron scattering plane and the hadron production plane. The unpolarized cross section for single-pion electroproduction can be written as [2]:

$$\frac{\partial^5\sigma}{\partial E_f \partial\Omega_e \partial\Omega^*_\pi} = \Gamma \cdot \frac{d\sigma}{d\Omega^*_\pi}, \tag{5}$$

$$\Gamma = \frac{\alpha}{2\pi^2 Q^2}\frac{(W^2 - M^2)E_f}{ME_i}\frac{1}{1-\epsilon}, \tag{6}$$

$$\frac{d\sigma}{d\Omega^*_\pi} = \sigma_T + \epsilon\sigma_L + \epsilon\sigma_{TT}\cos 2\phi + \sqrt{2\epsilon(1+\epsilon)}\sigma_{TL}\cos\phi, \tag{7}$$

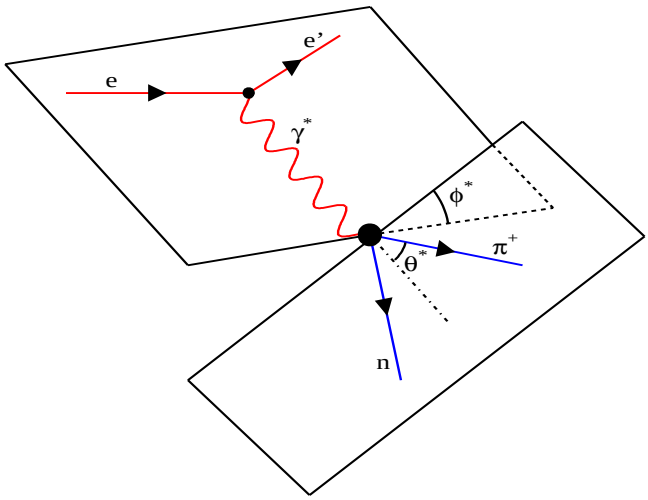

FIG. 1: (Color online) Kinematic diagram of single-pion electroproduction.

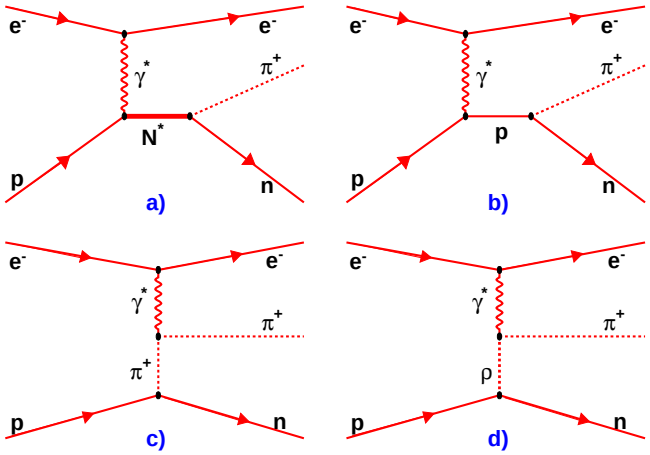

FIG. 2: (Color online) Some of the main diagrams contributing to single π^+ electroproduction.

where Γ is the virtual photon flux, and $\frac{d\sigma}{d\Omega^*_\pi}$ is the virtual photoproduction cross section. The σ_T, σ_L, σ_{TT} and σ_{TL} structure functions are bilinear combinations of the helicity amplitudes, depending only on the variables Q^2, W and θ. The analysis of the angular distributions provides information for extracting the electroproduction amplitudes for different resonances.

The main tree-level Feynman diagrams contributing to the $ep \to e'\pi^+ n$ process are shown in Fig. 2. The s-channel resonance excitation process is represented by the diagram in Fig. 2a. The hadronic vertex of this process is known from πN elastic scattering experiments [3]. Therefore studies of pion electroproduction can yield the Q^2 evolution of the photocoupling amplitudes describing the $\gamma^* NN^*$ vertex. For the purpose of studying the excitation of nucleon resonances, the other diagrams are considered as physical background. The largest non-resonant contribution to the cross section comes from the t-channel pion exchange diagram, shown in Fig. 2c. Although this process mainly contributes in the forward region due to the pion propagator pole, it still accounts for a significant part of the cross section even at large angles. The diagrams in Fig. 2b and Fig. 2d correspond to the s-channel nucleon pole and t-channel ρ-meson exchange amplitudes. Sophisticated analysis procedures are necessary to separate the resonant contributions from the non-resonant background, and to extract the resonant amplitudes for different overlapping excited states. The extraction of resonance multipoles is beyond the scope of this paper. In this contribution we describe the experiment and data analysis, and the extraction of fully exclusive and differential cross sections, and determination of response functions.

Electroexcitation of a nucleon resonance can be described in terms of three photocoupling amplitudes $A_{1/2}$, $A_{3/2}$ and $S_{1/2}$. The first two are due to the coupling of transverse photons with the proton resulting in a combined helicity $h = \frac{1}{2}$ or $h = \frac{3}{2}$ respectively. The $S_{1/2}$ amplitude is present due to the possibility of a longitudinal polarization for virtual photons. Alternatively, pion electroproduction can be described using multipole amplitudes $E_{l\pm}$, $M_{l\pm}$ and $S_{l\pm}$. The l-index represents the orbital angular momentum of the πN system, and the $\pm$ sign indicates how the nucleon spin is coupled to the orbital momentum. For each excited state the helicity amplitudes can be expressed in terms of multipole amplitudes and vice versa [2].

Quark models predict that the $\frac{E_{1+}}{M_{1+}}$ and $\frac{S_{1+}}{M_{1+}}$ ratios for the $P_{33}(1232)$ are small at low Q^2 [4, 5], while perturbative QCD predicts $\frac{E_{1+}}{M_{1+}} = 1$ and $\frac{S_{1+}}{M_{1+}}$ is independent of Q^2 as $Q^2 \to \infty$ [6]. A transition between these two regimes is expected at some finite Q^2. At low Q^2 the deviations of these ratios from zero can be interpreted as non-spherical deformation of the nucleon or the $\Delta(1232)$ [7]. Usually these ratios for $\Delta(1232)$ are obtained through measurements in the $\pi^0 p$ decay channel with an assumption that the uncertainty due to the isospin $I = \frac{1}{2}$ background is negligible. High quality data in the $\pi^+ n$ channel will enable us to separate the isospin $I = \frac{1}{2}$ and $I = \frac{3}{2}$ components of the transition form-factors for the $P_{33}(1232)$ and to determine these ratios with smaller uncertainties coming from non-resonant contributions.

The second resonance region is dominated by the three known isospin $I = \frac{1}{2}$ states, $P_{11}(1440)$, $D_{13}(1520)$ and $S_{11}(1535)$. These resonances, produced in electron-proton scattering, are twice as likely to decay through the $\pi^+ n$ channel than through $\pi^0 p$. Therefore, cross section measurements of the $ep \to e'\pi^+ n$ process are crucial for understanding the properties of these states. The nature of the $P_{11}(1440)$ resonance is not understood in the framework of the constituent quark model (CQM) [8],

and there are suggestions that the Roper resonance may be a hybrid state [9] or a small quark core with a large vector meson cloud [10]. The Q^2 evolution of the $A_{1/2}$ photocoupling amplitude for the Roper is predicted to be different for 3-quark and hybrid states. Previous analyses [11, 12] indicate a rapid fall-off of $A_{1/2}$ between $Q^2 = 0$ and $Q^2 = 0.5$ GeV^2, therefore high quality data in this region will be very valuable in understanding the nature of the $P_{11}(1440)$.

The experimental data for the $A_{1/2}$ transition amplitude for $S_{11}(1535)$ show a significantly slower Q^2 fall-off than predicted by constituent quark models. Most of these results are obtained through analysis of η-meson electroproduction data, where there can be no $I = \frac{3}{2}$ background. The proximity of the $S_{11}(1535)$ mass to the η-production threshold complicates the analysis of the data. High quality single π^+ data currently exist only at the photoproduction point, and there is very little data for non-zero Q^2. The results from analyses of pion and η photoproduction data are significantly different [13], and the source of these discrepancies is still not understood. New electroproduction data will allow for a similar comparison between the results from the two channels from CLAS to check the consistency of the analysis frameworks. These data will also allow for a future combined analysis of pion and η production data, which will provide more stringent constraints on the fit.

Until now there have only been three experiments [14, 15, 16] measuring single π^+ electroproduction cross section in the resonance regions in this range of Q^2. In all of these experiments the lack of angular coverage in the center-of-mass reference frame significantly reduced the sensitivity to the resonant amplitudes. The aim of the present experiment is to provide differential cross sections for the $\pi^+ n$ channel over a large kinematic region and with high statistical accuracy, that can be used together with other channels to obtain more reliable results on the resonance photocoupling amplitudes.

EXPERIMENT

The measurement was carried out using the CEBAF Large Acceptance Spectrometer (CLAS) [17] at the Thomas Jefferson National Accelerator Facility (Jefferson Lab), located in Newport News, Virginia. CLAS is a nearly 4π detector, providing almost complete angular coverage for the $ep \to e'\pi^+ n$ reaction in the center-of-mass frame. It is well suited for conducting experiments which require detection of two or more particles in the final state. Such a detector and the continuous beam produced by CEBAF provide excellent conditions for measuring the $ep \to e'\pi^+ n$ electroproduction cross section by detecting the outgoing electron and pion in coincidence.

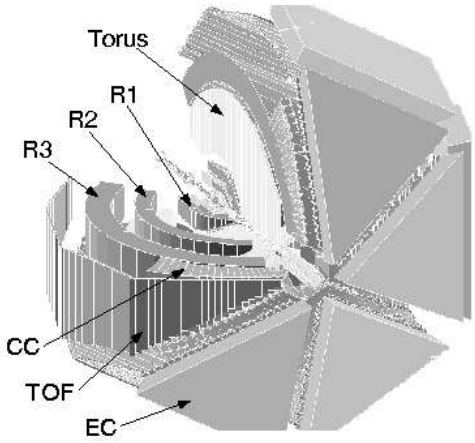

FIG. 3: Three dimensional view of CLAS.

Apparatus

The main magnetic field of CLAS is provided by six superconducting coils, which produce an approximately toroidal field in the azimuthal direction around the beam axis. The gaps between the cryostats are instrumented with six identical detector packages, also referred to here as "sectors", as shown in Fig 3. Each sector consists of three regions (R1, R2, R3) of Drift Chambers (DC) [18] to determine the trajectories of the charged particles, Čerenkov Counters (CC) [19] for electron identification, Scintillator Counters (SC) [20] for charged particle identification using the Time-Of-Flight (TOF) method, and Electromagnetic Calorimeters (EC) [21] used for electron identification and detection of neutral particles. The liquid-hydrogen target was located in the center of the detector on the beam axis. To reduce the electromagnetic background resulting from Møller scattering off atomic electrons, a second smaller normal-conducting toroidal magnet (mini-torus) was placed symmetrically around the target. This additional magnetic field prevented the Møller electrons from reaching the detector volume. A totally absorbing Faraday cup, located at the very end of the beam line, was used to determine the integrated beam charge passing through the target. The CLAS detector can provide $\frac{\delta p}{p} < 0.5\%$ momentum resolution, and $\approx 80\%$ of 4π solid-angle coverage. The efficiency of detection and reconstruction for stable charged particles in fiducial regions of CLAS is $\epsilon > 95\%$. The combined information from the tracking in the DC and the TOF systems allows us to reliably separate protons from positive pions for momenta up to 3 GeV.

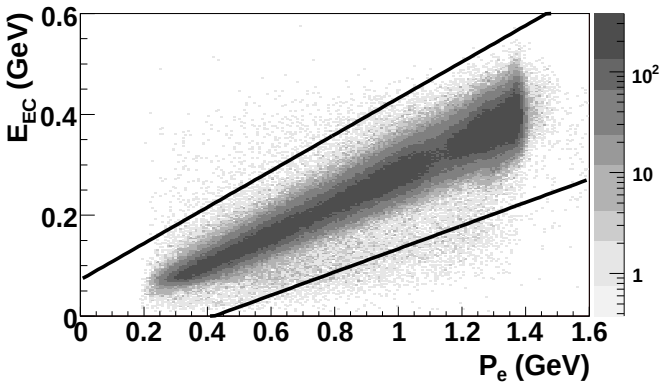

FIG. 4: Energy deposited by the electron candidates in the electromagnetic calorimeter versus their momenta. The black lines show the cut applied for the electron identification.

Data taking and data reduction

The data were taken in the spring of 1999 as part of the experimental program of the CLAS collaboration. The CEBAF 1.5 GeV electron beam was incident on a 5-cm long liquid hydrogen target at 20.5 K temperature. The data were taken at 3 nA nominal beam current, with ± 0.04 nA current fluctuations, at luminosities of $\sim 4 \times 10^{33}$ cm^{-2}s^{-1}. The size of the beam spot at the target was ~ 0.2 mm, with position fluctuations of ± 0.04 mm. The main torus current was set at 1500 A, which created a magnetic field of about 0.8 Tesla in the forward direction. The magnetic field of the spectrometer is significantly lower at large angles. The CLAS event readout was triggered by a coincidence of signals from the electromagnetic calorimeter and the Čerenkov counters in a single sector, generating an event rate of ~ 2 kHz. The total number of accumulated triggers at these detector settings was about 4.5×10^8. The raw data were written onto a tape silo of the Jefferson Lab Computer Center. During the off-line processing each file was retrieved from the tape silo and analyzed to produce files for general use containing 4-vectors of the reconstructed particles. ROOT [22] files, containing the specific information relevant for single π^+ electroproduction, were created and stored on a disk. These files were further analyzed to extract the differential cross sections for the $ep \to e'\pi^+ n$ reaction.

Particle identification

One of the key issues in electron scattering experiments is the ability of the detector to reliably identify electrons. Electron identification at the trigger level was accomplished by requiring a minimum amount of deposited energy in the electromagnetic calorimeter in coincidence with a signal in the Čerenkov counter in the same sector. Additional requirements were applied in the off-line analysis to select events containing an electron. First, a geometrical matching was required between the EC and CC hits and the associated negatively charged tracks in the drift chambers. The values of the geometrical cuts in the software are given in Table I. A sampling fraction cut was imposed on the dependence of the EC visible energy on the momentum to reject the background coming from negative pions (see Fig. 4). The electron identification in the off-line analysis can be summarized by:

Matching	Tolerance
$TRK \otimes EC$	30 cm
$TRK \otimes CC$	5^o
$EC \otimes CC$	5^o

TABLE I: Cuts for the geometrical matching in the offline analysis software.

$$EID = TRK \otimes CC \otimes EC \otimes SF, \qquad (8)$$

where TRK stands for track reconstruction in the drift chambers, CC and EC are the Čerenkov counter and the calorimeter geometrically matched hits and SF is the sampling fraction cut described above. In order to avoid inefficiencies due to the trigger threshold in the electromagnetic calorimeter, only events containing an electron with at least 500 MeV momentum were used in the analysis. In addition, fiducial cuts, discussed later, were applied to select only electrons in the regions where the Čerenkov counter efficiency was greater than 92%. The final cross sections were corrected for the remaining inefficiency of the Čerenkov counters [19].

Charged hadron identification in the CLAS detector is accomplished using the momentum determined from the tracking and the timing information from the scintillation counters. Fig. 5 shows the distribution of positively charged particles at 1.515 GeV electron beam energy plotted versus velocity β and momentum P. Bands due to positrons, pions, protons and deuterons can be easily identified. At low momentum the muon band is visible as well. The deuterons are produced from electron scattering on the aluminum windows of the target cell. All positive particles in the region outlined by the dashed lines were considered as π^+. Positrons can be separated from pions at low momenta, but at higher momenta the pion and positron bands merge. Background due to muons and positrons is significantly reduced by the missing mass and vertex cuts described below. The remaining contamination is evaluated as a systematic uncertainty.

Momentum corrections

When extracting the resonant parameters for excited states, it is important to have the correct value for the invariant mass of the hadronic state. Therefore, it is necessary to measure the electron momentum with high accuracy. For this reason additional corrections were applied to the electron momentum reconstructed by the standard CLAS software package. These corrections were determined using elastic scattering events from the same runs that were used in the single pion analysis. It was found that the missing mass determined from the elastically scattered electrons is typically ~ 5 MeV below the proton mass $M_p = 0.938$ GeV. Assuming that the scattering angle of the electron is measured correctly, and using:

$$E_f = \frac{2ME_i - (W^2 - M^2)}{2M + 4E_i \sin^2 \frac{\theta_e}{2}} \qquad (9)$$

the momentum correction factor can be found as:

$$C_p \equiv \frac{\delta E_f}{E_f} = -\frac{W^2 - M^2}{2ME_i}, \qquad (10)$$

where E_i is the electron beam energy and W is the measured recoil mass. This quantity was calculated for different bins in $\theta_e \in [15°, 55°]$ and $\phi_e^* \in [-30°, +30°]$ in the laboratory frame for each sector and stored in a look-up table. The azimuthal angle ϕ_e^* is defined within a sector, with $\phi_e^* = 0$ corresponding to the mid-plane of the sector. The momenta of the electrons from single π^+ production data were corrected using this table on an event-by-event basis. This procedure relies on the fact that the relative momentum offset is independent of W for a fixed value of θ_e. It was found that after these corrections were applied, the neutron peak in the missing mass of the $ep \to e'\pi^+X$ reaction was within ± 2.0 MeV of the neutron mass for 1.1 GeV$< W <$ 1.6 GeV range. Fig. 6 shows the difference between the missing mass in $ep \to e'\pi^+X$ reaction and the neutron mass with and without momentum corrections. The six gaps between the points are due to the six coils of the magnet. The dependence of the peak position on ϕ_e is practically eliminated by this procedure, and the peak is located much closer to the neutron mass.

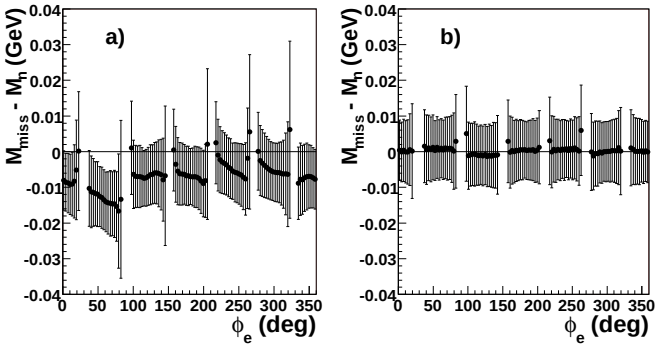

FIG. 6: Position of the missing mass peak in the $ep \to e'\pi^+X$ reaction versus ϕ_e in the lab frame: a) - before, b) - after momentum corrections are applied. The error bars represent the width of the distribution around the neutron mass.

Fiducial cuts

Although CLAS is a nearly 4π detector, it still contains significant inactive volumes without particle detectors. In addition, some of the detection inefficiencies in the ac-

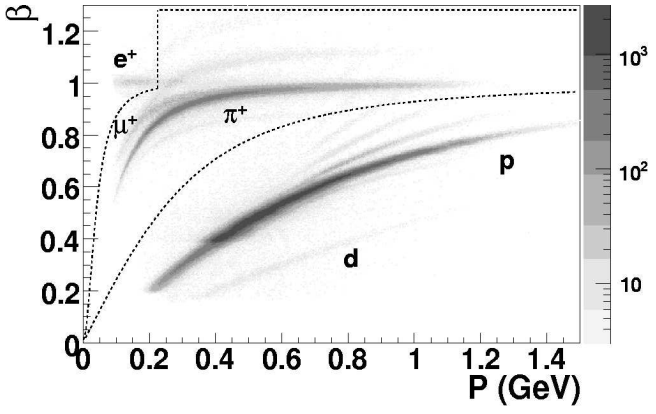

FIG. 5: Distribution of the number of positively charged particles versus β and p. The visible bands are due to positrons, muons, pions, protons and deuterons. All positive particles within the area outlined by the dashed lines are considered as π^+'s in this analysis.

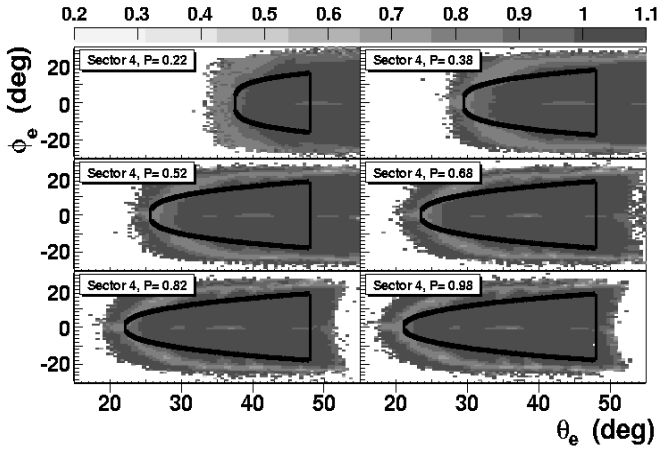

FIG. 7: Čerenkov counter efficiency versus the θ_e and ϕ_e electron angles in the laboratory frame for Sector 4. The black curves indicate the outer edges of the electron fiducial regions. Each momentum bin is 200 MeV wide.

tive volumes are not adequately reproduced in the detector simulation software. These areas are near the edges of the electromagnetic calorimeter, Čerenkov counter mirrors, the main torus and mini-torus coils, regions with broken wires in the drift chambers, and malfunctioning phototubes in the TOF system. To eliminate events with particles traveling through these regions, a set of fiducial cuts was developed. For electrons the main boundary of the fiducial region was defined by the efficiency of the Čerenkov counters and the edges of the electromagnetic calorimeter. Fig. 7 shows the dependence of the Čerenkov counter efficiency versus the θ_e and ϕ_e electron angles in the laboratory frame for six 200 MeV wide momentum bins in Sector 4. Due to the optics design of the CLAS Čerenkov counters [19] there are areas with relatively lower efficiency shown with the lighter shade. These features are difficult to implement in the detector simulation. Only events in the regions within the black curves and with the Čerenkov counter efficiency above 92% were used in the analysis. An additional set of geometrical cuts was applied to reject electrons hitting malfunctioning scintillator counters or traversing regions with missing or inefficient wires in the drift chambers.

Two sets of fiducial cuts were used to define the outer boundary of the fiducial regions for the positive pions. The first set, similar to the electron cuts, was defined in such a way that the ϕ_π^{lab} distributions of the number of events be uniform within the fiducial region. The second set of cuts was applied to ensure equivalent solid angle coverage for pions in the Monte-Carlo simulation and the real data. This mismatch was due to distortions of the minitorus coils which were not implemented in the detector simulation package. As in the case with the electrons, tracks in the regions with malfunctioning scintillator counters or broken wires were rejected by another set of fiducial cuts.

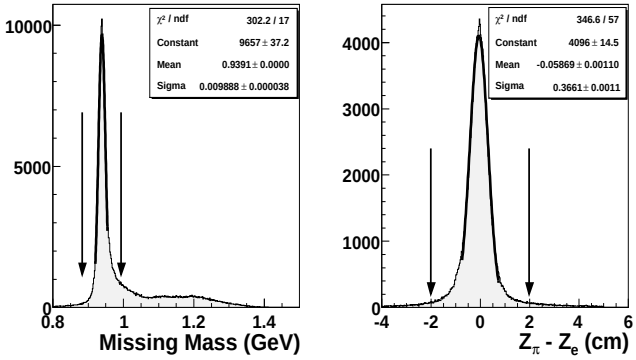

FIG. 8: Missing mass spectrum (a) and the distribution of the events versus $Z_\pi - Z_e$ (b). The arrows represent the cuts applied in the data analysis. The solid lines are gaussian fits to the data.

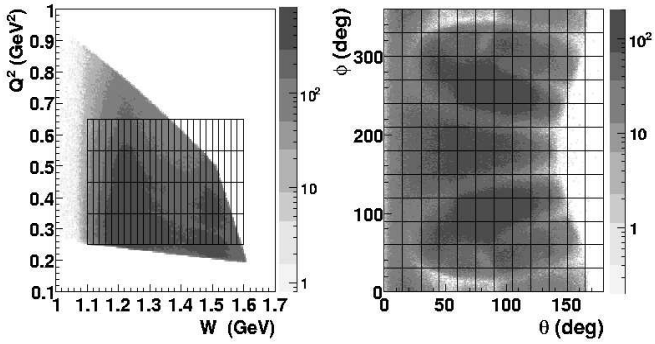

FIG. 9: Distribution of the number of single π^+ events versus: Q^2 and W - left; ϕ and θ center-of-mass angles - right.

Kinematic cuts

The exclusive final state was selected by detecting the outgoing electron and the π^+, and by requiring that the missing particle be a neutron. The missing-mass spectrum in Fig. 8a shows a prominent neutron peak as well as events from the radiative tail and from multi-pion production channels. The arrows indicate the cuts used in the analysis. The number of rejected events in the tails is recovered by imposing the same cuts on the simulated events in the acceptance calculations.

GEANT-based Monte-Carlo studies showed that about 18% of the positive pions decay in-flight into $\mu^+\nu_\mu$. Most of the momentum of the original pion is carried by the μ^+, which is, therefore, often detected and reconstructed as a π^+ with a significantly different momentum vector. In order to reduce the number of the events with decaying pions, a vertex cut $\mid Z_\pi - Z_e \mid < 2$ cm was applied on the difference of the Z-coordinates along the beam-line for the electron and the pion tracks in the same event (see Fig. 8b). This led to a reduction in the number of events with decaying π^+ to 4% with less than 1% losses in the number of events when the pion did not decay.

The kinematic coverage of this experiment is shown in Fig. 9. The grating on the figures shows the binning of the data. In the first resonance region this experiment covers a Q^2 range from 0.25 GeV^2 to 0.65 GeV^2, while in the second resonance region the upper boundary of the Q^2 coverage is reduced to 0.45 GeV^2. The angular coverage in the hadronic center-of-mass frame is nearly complete, with the exception of the region $\theta > 140°$. This limitation at larger angles is related to the fact that the CLAS coverage for charged particles is limited to 140° in laboratory frame. The number and the sizes of the cross section bins are given in Table II.

Variable	# of bins	Lower limit	Upper limit	Width
Q^2	4	0.25 GeV^2	0.65 GeV^2	0.10 GeV^2
W	25	1.1 GeV	1.6 GeV	20 MeV
θ	12	0°	180°	15°
ϕ	12	0°	360°	30°

TABLE II: The number and the sizes of the data bins. Values for the limits indicate the upper and lower edges of the bins, rather than the bin centers.

Acceptance corrections

In order to relate the experimental yields to cross sections, acceptance correction factors were calculated using the Monte-Carlo method. The GEANT-based detector simulation package GSIM incorporated the survey geometry of CLAS, realistic drift chamber and timing resolutions along with missing wires and malfunctioning photomultiplier tubes. Because CLAS is a complicated detector covering almost 4π of solid angle, it is virtually impossible to separate the efficiency calculations from the geometrical acceptance calculations. In this work the term acceptance correction refers to a combined correction factor due to the geometry of the detector and the inefficiencies of the detection and reconstruction. It is defined as the ratio of the number of reconstructed Monte-Carlo events to the number of simulated events in a given bin:

$$A = \frac{N_{rec}}{N_{sim}}. \tag{11}$$

With this definition of the acceptance it is desirable to have a realistic physics model in the event generator because of the finite bin sizes and bin migration effects, which are described later. In this work the MAID2000 model [23], which reasonably reproduces both $p\pi^0$ [24] and the current $n\pi^+$ CLAS data, was used as an input to the Monte-Carlo event generator. The simulated 200 million events were processed using the same software package and analyzed with the same cuts that were applied to the real data. An acceptance table with $8 \times 25 \times 24 \times 48$ bins in Q^2, W, θ and ϕ, respectively, was calculated using the definition in Eq. (11). The fine binning of the acceptance look-up table reduces the model dependence of the cross sections. The statistical errors for the acceptance corrections were estimated using the binomial distribution:

$$\delta A_{bin} = \sqrt{\frac{A_{bin}(1-A_{bin})}{N_{gen}-1}}, \tag{12}$$

where N_{gen} is the number of the Monte-Carlo events generated in the bin. These errors are included in the statistical error of the final cross sections.

The acceptance of CLAS for single-pion electroproduction at $Q^2 = 0.3$ GeV^2 and $W = 1.23$ GeV is shown in Fig. 10. The θ-dependence of the acceptance (see Fig. 10a) exhibits a dip at $\sim 45°$, which is due to the forward beam pipe. Six sectors of CLAS can be clearly identified in the plot showing acceptance versus ϕ-angle (see Fig. 10b). The width of the curves in these graphs represent the statistical error bands. Since a single cross section bin contains sixteen acceptance bins, the contribution of the acceptance statistical error to the total uncertainty of cross sections is on average approximately four times smaller than the errors seen in these plots.

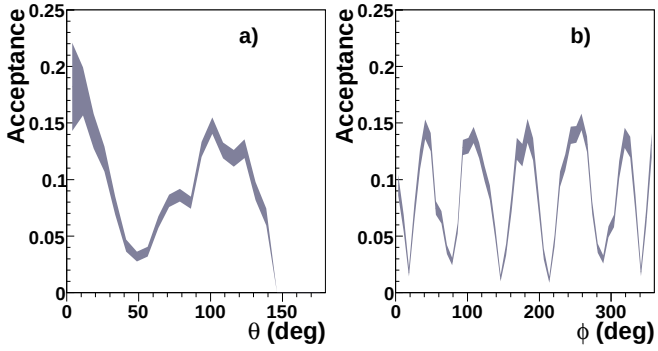

FIG. 10: Sample plots of acceptance corrections versus θ and ϕ pion angles in the center-of-mass frame in the $Q^2 = 0.3$ GeV^2 and $W = 1.23$ GeV bin. The θ-dependence (a) is shown at $\phi = 116.25°$ and the ϕ-dependence is at $\theta = 108.75°$. The width of the curves represent the statistical uncertainty for the acceptance.

Radiative corrections

In addition to processes which result in the exclusive $e'\pi^+ n$ final state, there are radiative processes represented by Feynman diagrams similar to the original single photon exchange diagrams, but with an additional photon leg, that also contribute to the cross sections. The experimentally measured cross sections must be corrected for such processes, also known as internal radiation. The radiative cross section for an exclusive process can be written as [25] :

$$d\sigma_r = \frac{(4\pi\alpha)^3 dQ^2 dW^2 d\Omega_\pi^*}{2(4\pi)^7 S^2 W^2} \times \int d\Omega_k dv \frac{v\sqrt{\lambda_W}}{f_W^2 Q^4} L_{\mu\nu}^{(r)} W_{\mu\nu}, \tag{13}$$

where $S \equiv 2E_i M_p$, $d\Omega_\pi^*$ is the differential center-of-mass solid angle of the π^+, $v \equiv M_X^2 - M_n^2$, $L_{\mu\nu}^{(r)}$ and $W_{\mu\nu}$ are the leptonic and the hadronic tensors respectively, and

$$\lambda_W \equiv (W^2 - m_{\pi^+}^2 - M_{miss}^2)^2 - 4m_{\pi^+}^2 W^2 \tag{14}$$

$$f_W \equiv W - E_\pi + p_\pi(\cos\theta_\pi \cos\theta_k + \sin\theta_\pi \sin\theta_k \cos(\phi_\pi - \phi_k)). \tag{15}$$

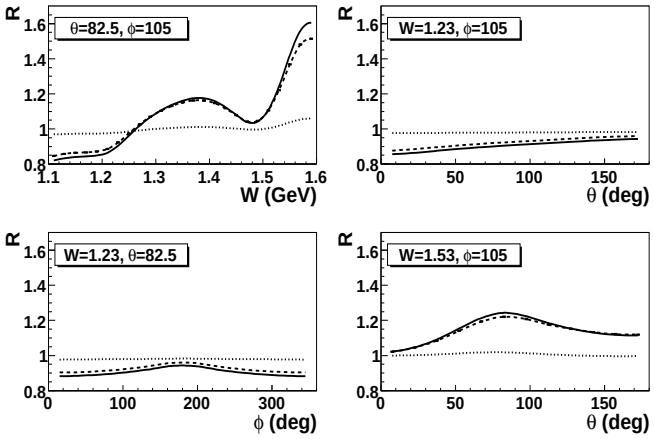

FIG. 11: Sample plots of the radiative correction factor R at $Q^2 = 0.3\,\mathrm{GeV}^2$. The dotted lines are the external corrections, the dashed lines are internal corrections, and the solid lines show the combined radiative correction.

Here, θ_π, ϕ_π, θ_k and ϕ_k are the pion and radiated photon's angles in the hadronic center-of-mass reference frame. The integral in Eq. (15) is taken over the photon angles and variable v.

In addition, there is also a nonzero probability that in the presence of the electromagnetic field of the atoms of the target the electron will emit one or more photons before or after interacting with the nucleus of the target (external radiation). The probability of emitting a real photon of a particular energy is proportional to the path length of the electron in the target material. The size of the external radiative corrections for these measurements was significantly smaller than for internal because of the small amount of the target material ($t = 0.5\%$ of radiation length).

The internal radiative corrections for the cross sections were calculated using the *ExcluRad* program [25] as multiplicative correction factors for each data bin. The external radiative corrections were done using the Mo and Tsai formalism [26]. The unradiated structure functions, needed as an input for the correction procedure, were calculated using a parameterization of the multipole amplitudes using a fit of these CLAS data based on the unitary isobar model [27]. The size of the required corrections varied up to 55%, depending on the kinematics. Fig. 11 shows dependences of the radiative corrections $R \equiv \frac{\sigma_{rad}}{\sigma_{Born}}$ on the variables W, θ and ϕ at $Q^2 = 0.3\,\mathrm{GeV}^2$. The dotted line shows the correction due to external radiation, and the dashed line is the correction factor obtained using the *ExcluRad* program. The solid line is the combined correction factor calculated as the product of the two. Because of the short length of the target, the external radiative corrections are much smaller than the internal corrections.

Corrections for binning effects

Because of the finite detector resolution and finite bin size, the measured values of the cross section in the center of the data bin can be distorted by up to 10%. The experimentally measured quantity is the cross section averaged over a full data bin, while usually it is more desirable to determine the value of the cross section at the center of the bin. To account for such distortions, multiplicative corrections were introduced as the ratio of the cross section in the center of a bin to the average cross section in that bin:

$$B = \frac{\frac{d\sigma}{d\Omega^*_\pi}\,|_{ctr}}{\frac{d\sigma}{d\Omega^*_\pi}\,|_{avg}}. \qquad (16)$$

The averaged cross sections were evaluated using two models: the Q^2 dependence of the cross sections was taken from the MAID2000 model [23], while the cross sections at fixed values of Q^2 were obtained using a unitary isobar [27] fit to these data in the first iteration.

Normalization

The integrated charge of the electron beam passing through the target was measured using the Faraday cup located at the end of the Hall B beam line. It generated pulses with a frequency proportional to the beam current with 10 Hz per 1 nA linear slope parameter. The calibration parameters of this device are known with less than 0.5% uncertainty. The measured charge was corrected for the data acquisition live-time, calculated as the ratio of the counts from two scalers. These scalers were connected to a single 100 kHz pulse generator. One of them was ungated, while the other one was gated by the data acquisition "live" signal. To ensure the quality of the analyzed data sample, software cuts were imposed on the live-time, elastic scattering and single π^+ electroproduction rates. The portions of the runs for which these quantities were outside of the imposed limits were excluded from the analysis, with the corresponding beam charge being subtracted from the total charge. As was mentioned above, the Čerenkov counter efficiencies were parameterized during the calibration procedure [19], and the appropriate corrections were applied to the cross sections. The comparison of the elastic scattering cross sections versus θ_e from CLAS and the model calculation using a parameterization [28] for the elastic form factors is shown in Fig. 12. The model cross section includes radiative effects, according to the Mo and Tsai formalism [26]. The error bars on the data points represent statistical uncertainties only. The solid line at $R = 1.015$ shows the result of fitting a constant to the ratio of the measured cross sections to the parameterization [28]. The fluctuations around this line can be used to estimate the

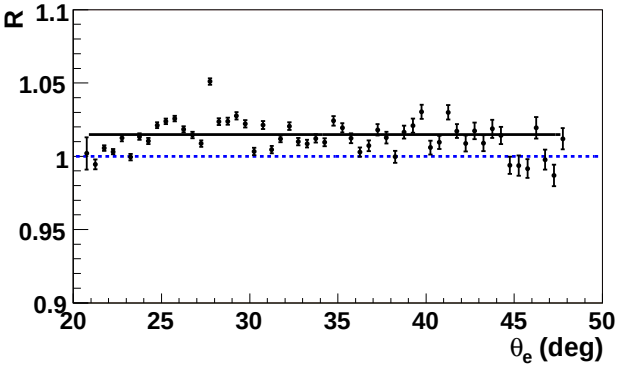

FIG. 12: The ratio of the measured elastic cross section to the parameterization of the world data [28]. The error bars represent the statistical uncertainty only. The solid line is from the fit of the data points to a constant.

systematic uncertainty of electron detection and reconstruction.

The contributions from scattering off the target cell walls was estimated to be 1.5% using empty target runs. This correction factor was applied to the cross section in every data bin.

SYSTEMATIC ERRORS STUDIES

A number of studies were carried out to estimate the systematic uncertainties on the measured cross sections. The primary method used in these studies was to vary different independent parameters of the analysis to determine the corresponding change in the resulting cross sections and the structure functions.

Because of the finite bin size, the result of averaging the acceptance over an acceptance bin depends on the distribution of events in that bin. If the physics model used in the Monte-Carlo simulation differs from the real data, then the averaging over a bin may result in an incorrect cross section. The introduced error depends on the shape of the acceptance function and the cross sections as well as on the acceptance bin size. In addition, because of the finite detector resolution, some of the events produced in one acceptance bin will be reconstructed in a different bin. This may cause significant distortions in the final cross section distributions. In order to correctly account for these effects, a realistic physics generator and detector simulation are required. To estimate the errors of the final results due to the model used in the acceptance calculations, we calculated the acceptance table with two different models. The comparison of the results with the two acceptance corrections allowed us to estimate the systematic errors due to the physics model in the acceptance calculations.

As was mentioned above, we use missing mass and vertex cuts to select the single-pion production events and to reduce the number of events with decaying pions. These cuts cause losses of some single-pion events as well. The true number of events is expected to be recovered by applying the acceptance corrections by using exactly the same cuts on the Monte-Carlo data. The remaining systematic errors associated with these cuts were estimated by varying the sizes of the windows. The absolute value of the cross section variations calculated with different cut windows, averaged over ϕ at fixed Q^2, W and θ, was considered as the systematic uncertainty for all ϕ for that fixed Q^2, W and θ.

One of the possible sources of systematic errors in this experiment is the uncertainty in the normalization. This can arise from miscalibrations of the Faraday cup, target density variations, errors in determining the target length and its temperature along with data acquisition live-time and other factors. However, the presence of the elastic events in the data set allows us to account for the normalization uncertainties of the cross sections by comparing the elastic cross sections to the parameterization of the world data [28]. This way we were able to combine the normalization, electron detection, electron tracking and electron identification errors into one global uncertainty factor. A comparison of the measured elastic cross sections for different θ_e and ϕ_e electron angles allowed us to assign a 5.2% global uncertainty due to the normalization and electron efficiency uncertainties.

The systematic uncertainty due to the model used in the radiative corrections was estimated by performing a second iteration. The radiatively corrected experimental cross sections from CLAS were fitted once more, and using the fit the new correction factors were calculated and compared with the previous iteration. The comparison indicated an uncertainty on the order of 2% due to the model dependence of the radiative corrections.

Using the kinematically over-determined reaction $ep \to e'\pi^+\pi^- p$ allows us to determine the π^+ efficiency by detecting the outgoing electron, π^- and proton. The efficiency of the π^+ detection can be found as the ratio of the number of events where the π^+ was detected to the number of events where the π^+ was expected to be detected. A comparison of the pion efficiency calculated from the real data with the efficiency from GEANT-based Monte-Carlo simulation lead to a systematic error estimate of 2.5%.

In order to estimate the background coming from two-pion production, a sample of two-pion Monte-Carlo events was processed as if it were the actual data sample. The analysis of these events showed that this background would contribute less than 1% uncertainty to the differential cross sections. The systematic error due to the π^+ misidentification was estimated to be about $\sim 0.5\%$ by varying the cut in the proton-pion separation in the

analysis.

The total systematic error in each bin was calculated as the square root of the sum of the squares of these different contributions. The size of the systematic errors is typically slightly larger than the size of the statistical uncertainties and is shown in Fig. 13 as the shaded bands.

RESULTS

Cross sections

The experimental differential cross section for each data bin was determined using the following formula:

$$\frac{\partial^5\sigma}{\partial E_f \partial\Omega_e \partial\Omega^*_\pi} = R\cdot B \sum_{events} \frac{1}{AL\epsilon_{cc}}\cdot$$
$$\cdot\frac{1}{\Delta Q^2 \Delta W \sin\theta \Delta\theta\Delta\phi}\cdot\frac{\partial(W,Q^2)}{\partial(E_f,\cos\theta_e)}, \qquad (17)$$

$$L = \frac{Q_{tot}}{e} N_A \rho L_T, \qquad (18)$$

$$\frac{\partial(W,Q^2)}{\partial(E_f,\cos\theta_e)} = \frac{2ME_iE_f}{W}, \qquad (19)$$

where the sum in Eq. 17 runs over the $e\pi^+(n)$ events reconstructed in the fiducial region of CLAS. Here A is the acceptance correction factor for an event, L is the integrated luminosity, N_A is Avogadro's number, ρ is the target density, L_T is the target length, Q_{tot} is the integrated charge corrected for the data acquisition livetime, e is the electron charge, ϵ_{cc} is the Čerenkov efficiency correction factor, ΔQ^2, ΔW, $\Delta\theta$, $\Delta\phi$ are the bin sizes, $\frac{\partial(W,Q^2)}{\partial(E_f,\cos\theta_e)}$ is the Jacobian between the (W,Q^2) and $(E_f,\cos\theta_e)$ sets of variables, and R and B are the radiative and binning correction factors, respectively. The values of all kinematic variables are calculated for each particular event, as opposed to being taken at the center of the bin. The virtual photoproduction cross section can be obtained, according to Eq. (5), by dividing the left-hand side of Eq. (17) by the virtual photon flux Γ factor defined in Eq. (6). Sample plots of the differential cross sections compared with models are shown in Fig. 13. The solid line shows the cross sections calculated using MAID2003 [29] multipoles with $l \leq 5$ (here simply referred to as MAID2003 model). The MAID model uses effective Langrangian approach to calculate the Born background, including ω and ρ meson calculations. The background is unitarized in the K-matrix approximation. The resonant amplitudes are determined by fitting the world pion production data. The dashed line in Fig. 13 corresponds to the model by Sato and Lee [30]. This model obtains an effective Hamiltonian from the interaction Lagrangian using the method of unitary transformations. Due to complicated calculations Sato-Lee model only includes the $P_{33}(1232)$ resonance and, therefore, it's validity domain is limited to the first resonance region. The shaded areas at the bottom represent the estimated systematic uncertainties. Typically the systematic uncertainties are slightly larger than the statistical errors. The data and the models are globally in qualitative agreement, while in certain regions there are quantitative discrepancies. Due to the large number of data points, it is more convenient in this paper to discuss the structure functions rather than the cross sections themselves. The values of the measured cross sections will be available from the CLAS physics database [31] or upon request [32] .

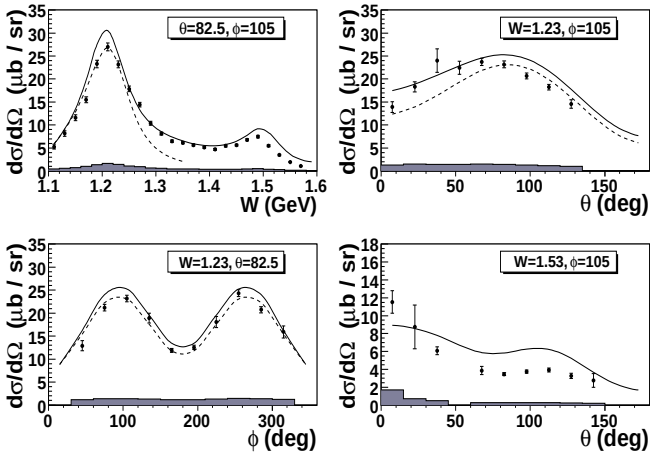

FIG. 13: Sample plots of π^+ virtual photoproduction cross sections at $Q^2 = 0.3$ GeV^2 for different kinematics. The shaded bands represent the systematic uncertainties. The solid curve is MAID2003 [29] , and the dashed curve is a calculation from Sato-Lee [30].

Structure functions

The structure functions σ_{TT}, σ_{TL} and the linear combination $\sigma_T + \epsilon\sigma_L$ were obtained by fitting the ϕ-dependence of the cross section to a function of the form:

$$F(\phi) = A + B\cos\phi + C\cos 2\phi. \qquad (20)$$

The large angular coverage of CLAS in the center-of-mass reference frame allowed us to extract the structure functions up to 145° in the center-of-mass θ angle. The W and θ dependencies of the structure functions are shown in Fig. 14 and Appendix A. The solid curves in Fig. 14 and Appendix A are from MAID2003 [29] calculations, while the dashed curves are from the Sato-Lee model [30]. The table of the structure functions are presented in Appendix B. The error column in the table shows the statistical and systematic uncertainties added in quadrature.

A typical W-distribution of the $\sigma_T + \epsilon\sigma_L$ and σ_{TT} terms features a distinct $\Delta(1232)$ peak, followed by the less prominent second resonance region. The θ-dependence of $\sigma_T + \epsilon\sigma_L$ is mostly flat at low values of W near the single-pion production threshold. This is consistent with E_{0+} dominance at low energies. With increasing invariant mass, structures are developing at $\theta \approx 90°$, which is characteristic of resonance production. Above the first resonance region the θ-dependence of $\sigma_T + \epsilon\sigma_L$ becomes monotonically falling, consistent with the t-channel pion exchange mechanism dominance.

From the plots in Figs. 19,21,23,25 in Appendix A, one can see that in the first resonance region the measurements of σ_{TT} agree very well with the Sato-Lee [30] model. For these values of hadronic center-of-mass energy this structure function is dominated by the $\Delta(1232)$ resonance contributions. But the model predictions for the $\sigma_T + \epsilon\sigma_L$ linear combination disagree with the measured values, although the discrepancy is within the systematic errors. The present experiment does not separate the longitudinal and transverse structure functions. Given the successful description of the σ_{TT} term, which can be expressed in terms of helicity amplitudes as $\sigma_{TT} \sim Re(H_3 H_2^* - H_4 H_1^*)$, one may assume that the structure function $\sigma_T \sim |H_1|^2 + |H_2|^2 + |H_3|^2 + |H_4|^2$, which depends on the same helicity amplitudes, may also be described reasonably well. Then the discrepancies in the sum $\sigma_T + \epsilon\sigma_L$ could be due to incomplete knowledge of the non-resonant physical background contributing directly to σ_L. Therefore, these data can be used to improve our understanding of the non-resonant background in the first resonance region. The measured σ_{TL} structure function is the smallest, and the relative systematic uncertainties are large. The predictions for σ_{TL} from Sato-Lee [30] are in agreement with the measured values within the error bars.

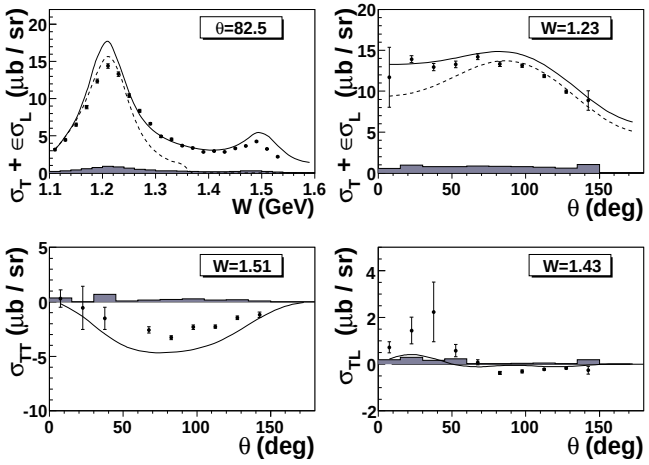

FIG. 14: Sample plots of structure functions from CLAS at $Q^2 = 0.4$ GeV^2. The solid curves are from MAID2003 [29] and the dashed curves are from the Sato-Lee calculations [30]. The shadowed areas show the systematic uncertainty.

The MAID2003 model, which is a fit to predominantly $\pi^0 p$ channel, describes our data surprisingly well, with the curves in the plots following most of the features of the experimental data. But the absolute values for the σ_{TT} and $\sigma_T + \epsilon\sigma_L$ structure functions are typically overestimated, especially in the second resonance region. This may be indicative of our relatively poor knowledge of the $D_{13}(1520)$ and $S_{11}(1535)$ strength in the $ep \to e'\pi^+ n$ channel. We also observe a distinct structure in the θ dependence of the σ_{TL} amplitude for $W > 1.32$ GeV, which is not reproduced by MAID2003, where the sign is in fact opposite (see Fig. 14). Inclusion of these data in the MAID fit can improve our knowledge of the resonance parameters, background terms and the branching ratios for the states in the second resonance region.

SUMMARY

In conclusion, for the first time we have measured the unpolarized electroproduction cross sections for the $ep \to e'\pi^+ n$ process covering a large angular range in the center-of-mass frame, and we have extracted the σ_{TT}, σ_{TL} and $\sigma_T + \epsilon\sigma_L$ linear combinations of the structure functions. The combined statistical and systematic errors are of the order of 10% in most of the measured kinematic region. In the first resonance region the measured cross sections and the structure functions are in qualitative agreement with the MAID2003 [29] and the Sato-Lee [30] models, with a quantitative discrepancy with the MAID2003 model [29]. In the second resonance region MAID2003 overestimates the height of the resonance peak. Together with $p\pi^0$ channel these data will provide the basis for the analysis of resonance transition form-factors in a coupled-channel analysis.

Acknowledgments

We would like to thank the staff of the Accelerator and Physics Divisions at the Jefferson Laboratory for their outstanding efforts to provide us with the high quality beam and the facilities for the data analysis. This work was supported by the U.S. Department of Energy and the National Science Foundation, the French Commissariat à l'Energie Atomique, the Italian Istituto Nazionale di Fisica Nucleare, and the Korean Science and Engineering Foundation. The Southeastern Universities Research Association (SURA) operates the Thomas Jefferson National Accelerator Facility for the United States Department of Energy under Contract No. DE-AC05-84ER40150.

* Current Address: Sakarya University, Sakarya, Turkey

[1] V. Burkert, T.-S.H. Lee, Int. J. Mod. Phys. **E13**, 1035, 2004.
[2] F. Foster and G. Hughes, Rept. Prog. Phys. **46**, 1445, 1983.
[3] R.A. Arndt *et al.*, Phys. Rev. C**69**, 035213, 2004.
[4] N. Isgur *et al.*, Phys. Rev. D**25**, 2394, 1982.
[5] S. Capstick and G. Karl, Phys. Rev. D**41**, 2767, 1990.
[6] C.E. Carlson, Phys. Rev. D**34**, 2704, 1986.
[7] A.J. Buchmann and E.M. Henley, Phys. Rev. C**63**, 015202, 2001.
[8] N. Isgur, Acta Austriaca, Suppl. XXVII, 177, 1985.
[9] Zh. Li, V. Burkert, Zh. Li, Phys. Rev. D**46**, 70, 1992.
[10] F. Cano and P. Gonzales, Phys. Lett. **B431**, 270, 1998.
[11] R. Arndt *et al.*, Phys. Rev. C**66**, 055213, 2002.
[12] Ch. Gerhard, Z. Phys **C4**, 311, 1980.
[13] K. Hagiwara *et al.*, Phys. Rev. D**66**, 010001, 2002.
[14] E. Evangelides *et al.*, Nucl. Phys. **B71**, 381, 1974.
[15] H. Breuker *et al.*, Nucl. Phys. **B146**, 285, 1978.
[16] H. Breuker *et al.*, Z. Phys. **C13**, 113, 1982.
[17] B. Mecking *et al.*, Nucl. Inst. and Meth. **A503**, 513, 2003.
[18] M.D. Mestayer *et al.*, Nucl. Inst. and Meth. **A449**, 81, 2000.
[19] G. Adams *et al.*, Nucl. Inst. and Meth. **A465**, 414, 2001.
[20] E.S. Smith *et al.*, Nucl. Inst. and Meth. **A432**, 265, 1999.
[21] M. Amarian *et al.*, Nucl. Inst. and Meth. **A460**, 239, 2001.
[22] R. Brun and F. Rademakers, Nucl. Inst. and Meth. **A389**, 81, 1997.
[23] D. Drechsel *et al.*, Nucl. Phys. **A645**, 145, 1999.
[24] K. Joo *et al.*, Phys. Rev. Lett. **88**, 122001, 2002.
[25] A. Afanasev *et al.*, Phys. Rev. D**66**, 074004, 2002.
[26] L.W. Mo and Y.S. Tsai, Rev. Mod. Phys. **41**, 205, 1969.
[27] I.G. Aznauryan, Phys. Rev. C**67**, 015209, 2003.
[28] P.E. Bosted, Phys. Rev. C **51**, 409, 1995.
[29] L. Tiator *et al.*, Eur. Phys. J. **A19**, 25, 2004.
[30] T. Sato and T.-S.H. Lee, Phys. Rev. C **54**, 2660, 1996.
[31] http://clasweb.jlab.org/physicsdb/intro.html
[32] e-mail: Hovanes.Egiyan@jlab.org

APPENDIX A: PLOTS OF THE STRUCTURE FUNCTIONS

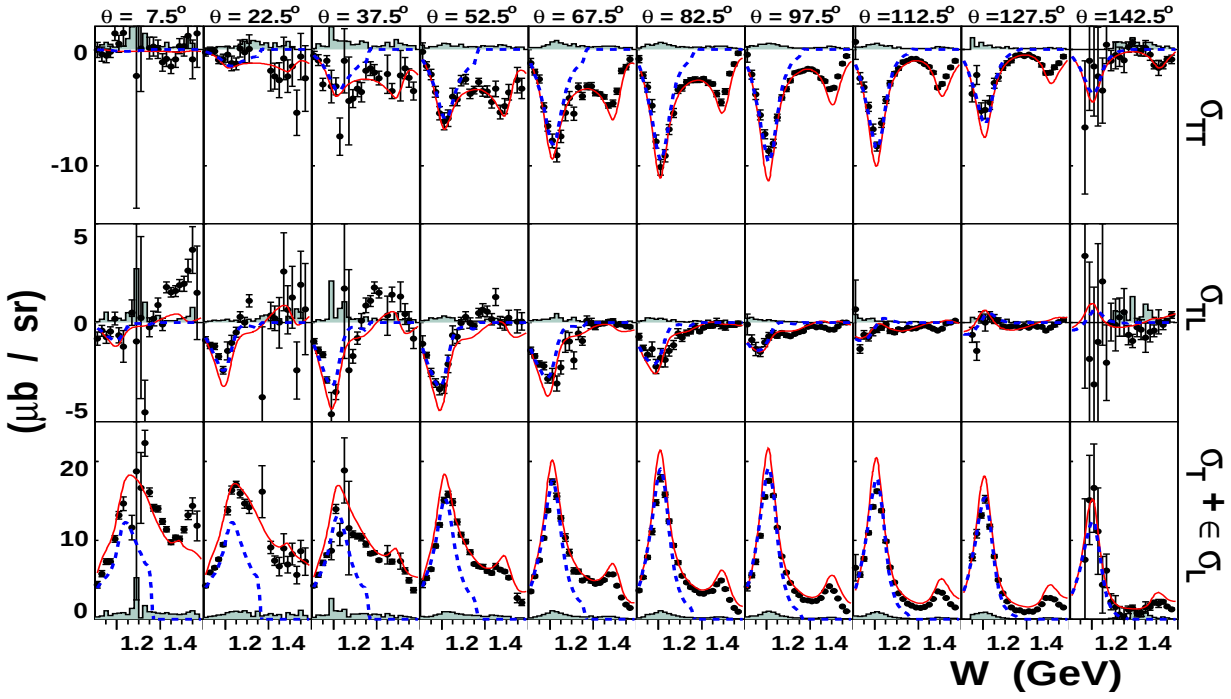

FIG. 15: (Color online) Structure functions versus W at $Q^2 = 0.3$ GeV^2. Solid curves represent MAID2003 calculations, while the dashed curves show the predictions of the Sato-Lee model. Shaded areas represent the systematic uncertainties.

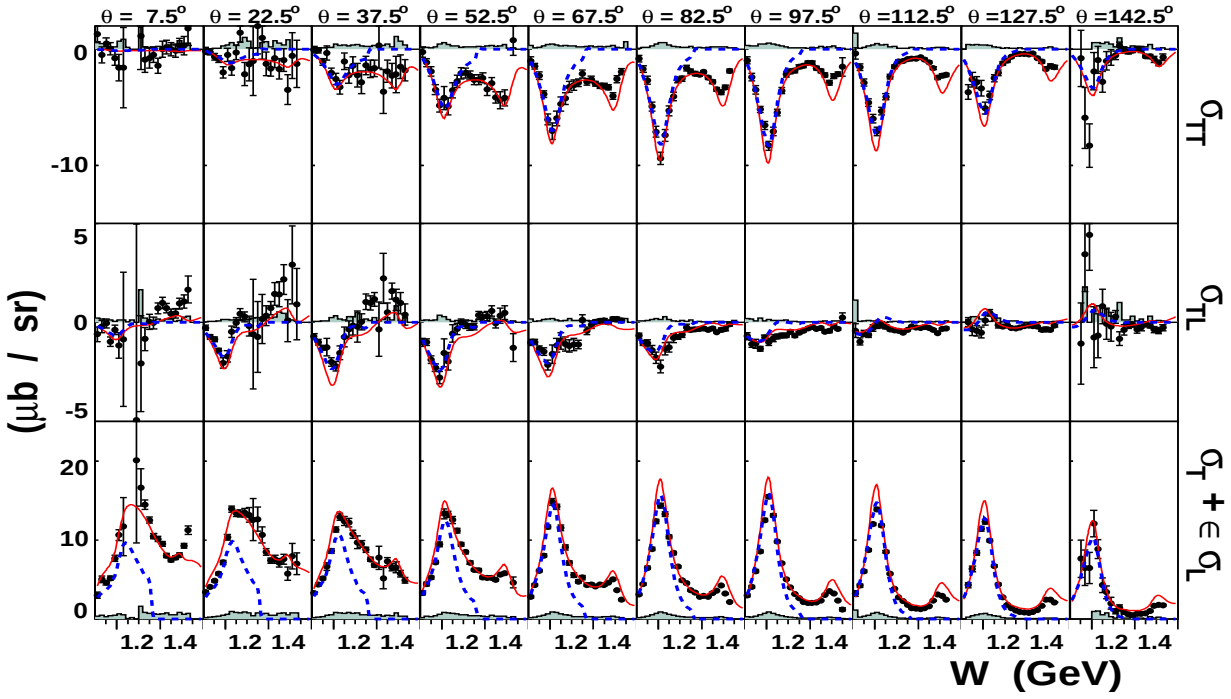

FIG. 16: (Color online) Structure functions versus W at $Q^2 = 0.4$ GeV^2. Solid curves represent MAID2003 calculations, while the dashed curves show the predictions of the Sato-Lee model. Shaded areas represent the systematic uncertainties.

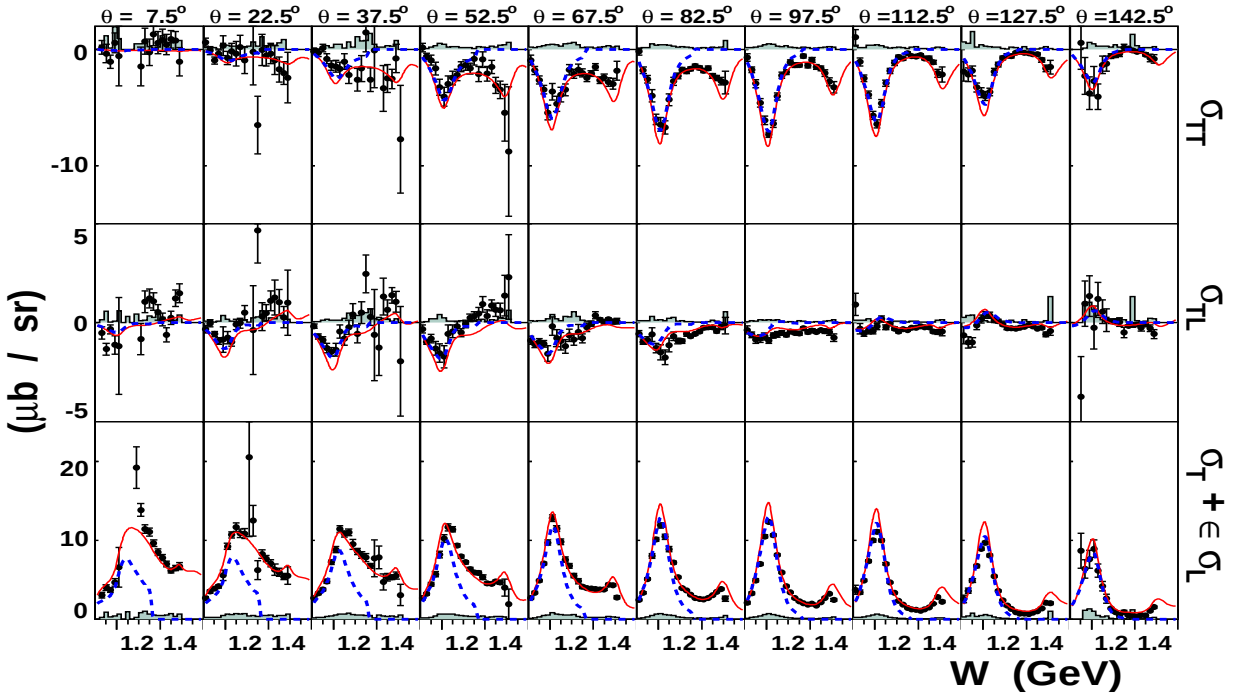

FIG. 17: (Color online) Structure functions versus W at $Q^2 = 0.5$ GeV^2. Solid curves represent MAID2003 calculations, while the dashed curves show the predictions of the Sato-Lee model. Shaded areas represent the systematic uncertainties.

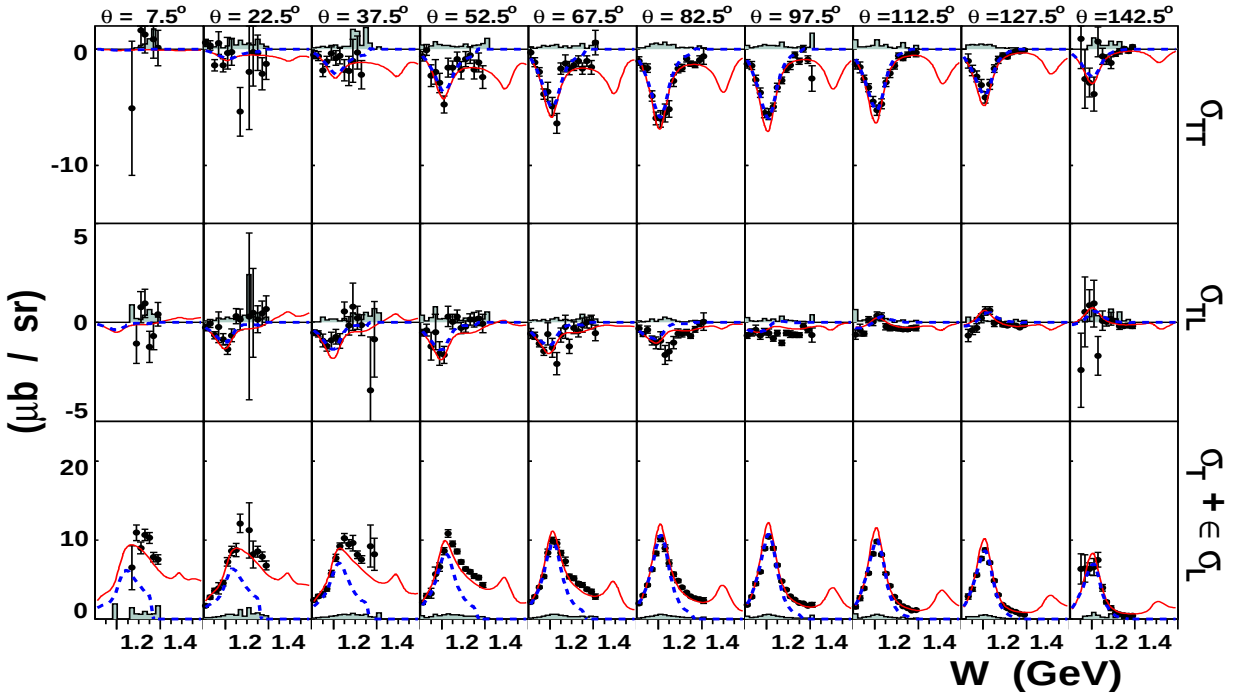

FIG. 18: (Color online) Structure functions versus W at $Q^2 = 0.6$ GeV^2. Solid curves represent MAID2003 calculations, while the dashed curves show the predictions of the Sato-Lee model. Shaded areas represent the systematic uncertainties.

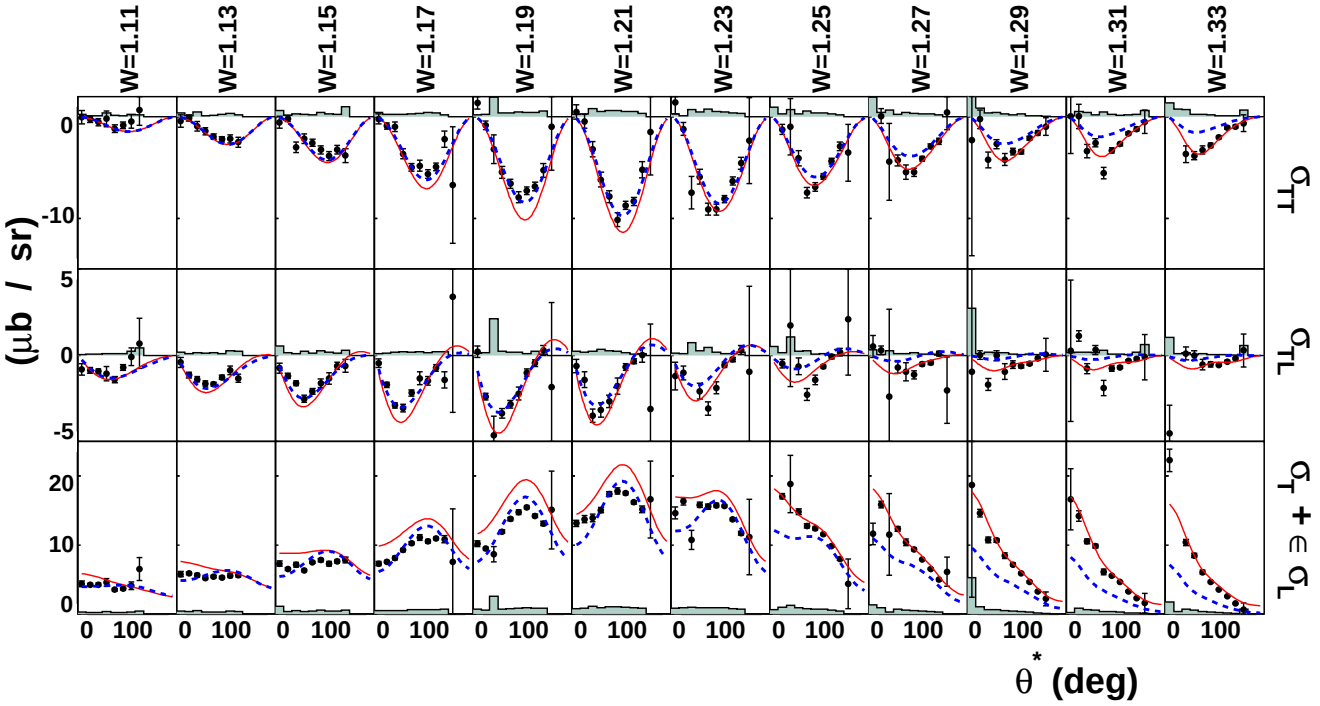

FIG. 19: (Color online) Structure functions versus c.m. θ at $Q^2 = 0.3$ GeV^2. Solid curves represent MAID2003 calculations, while the dashed curves show the predictions of the Sato-Lee model. Shaded areas represent the systematic uncertainties.

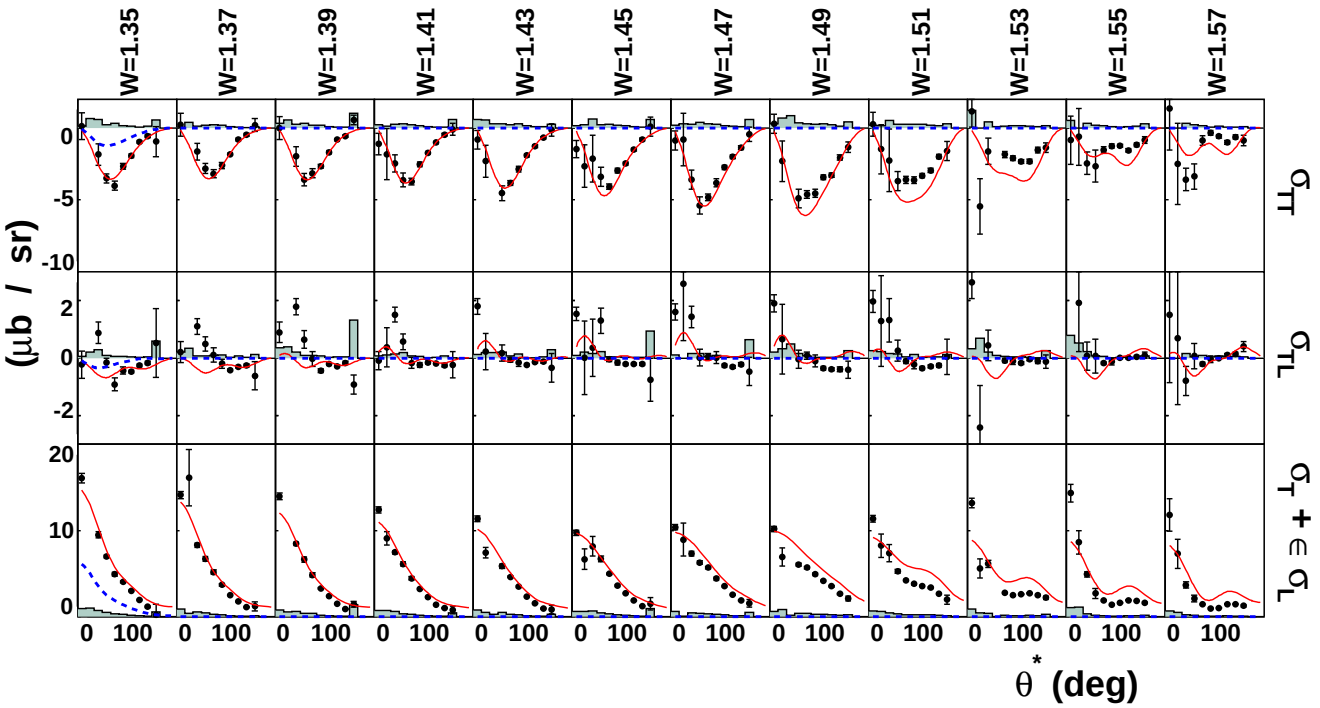

FIG. 20: (Color online) Structure functions versus c.m. θ at $Q^2 = 0.3$ GeV^2. Solid curves represent MAID2003 calculations, while the dashed curves show the predictions of the Sato-Lee model. Shaded areas represent the systematic uncertainties.

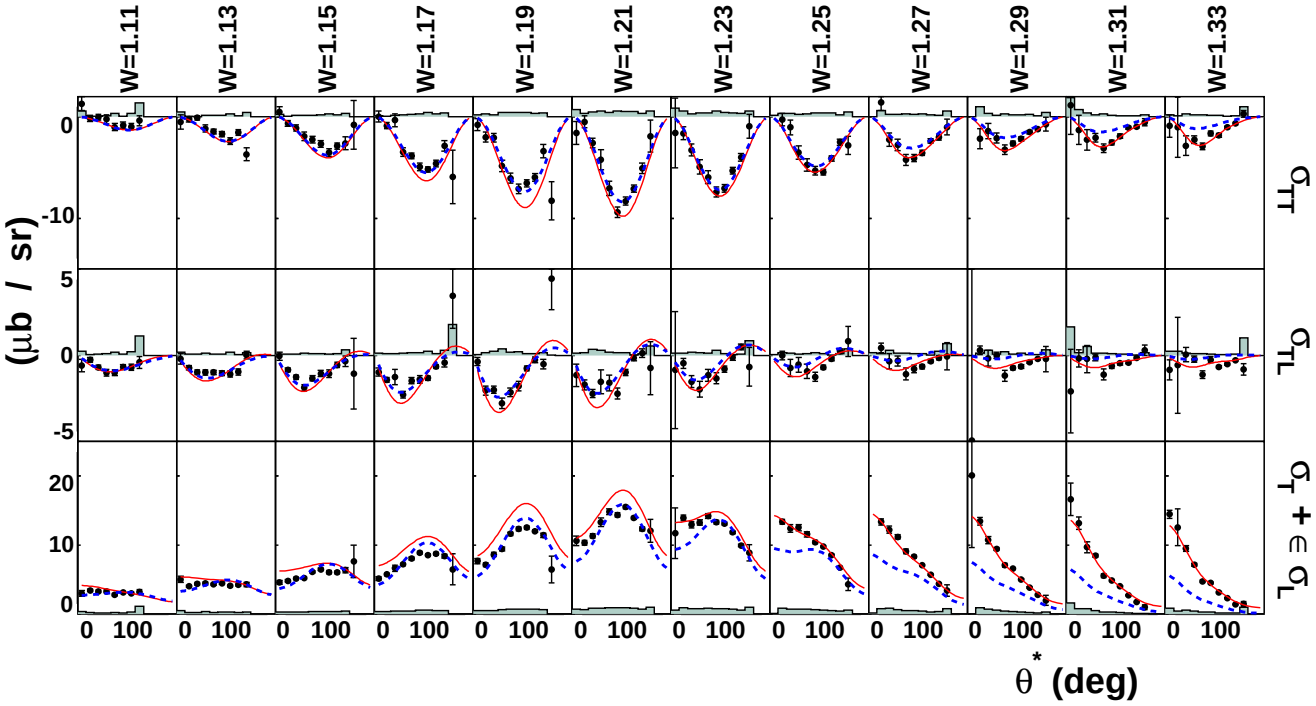

FIG. 21: (Color online) Structure functions versus c.m. θ at $Q^2 = 0.4$ GeV^2. Solid curves represent MAID2003 calculations, while the dashed curves show the predictions of the Sato-Lee model. Shaded areas represent the systematic uncertainties.

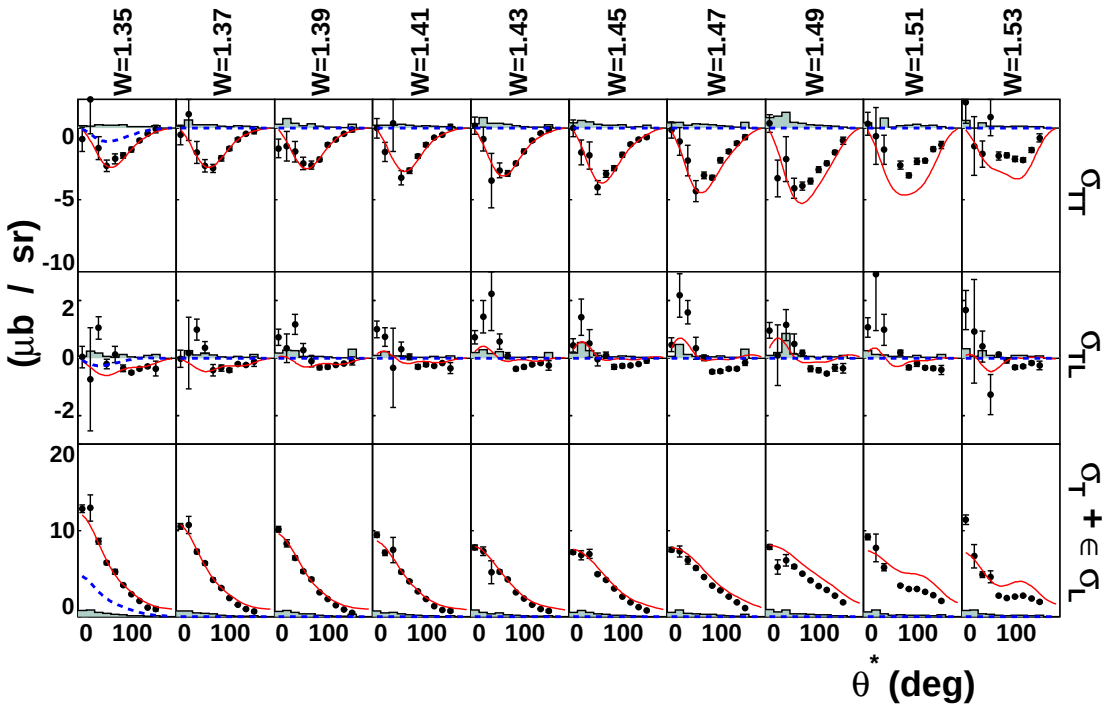

FIG. 22: (Color online) Structure functions versus c.m. θ at $Q^2 = 0.4$ GeV^2. Solid curves represent MAID2003 calculations, while the dashed curves show the predictions of the Sato-Lee model. Shaded areas represent the systematic uncertainties.

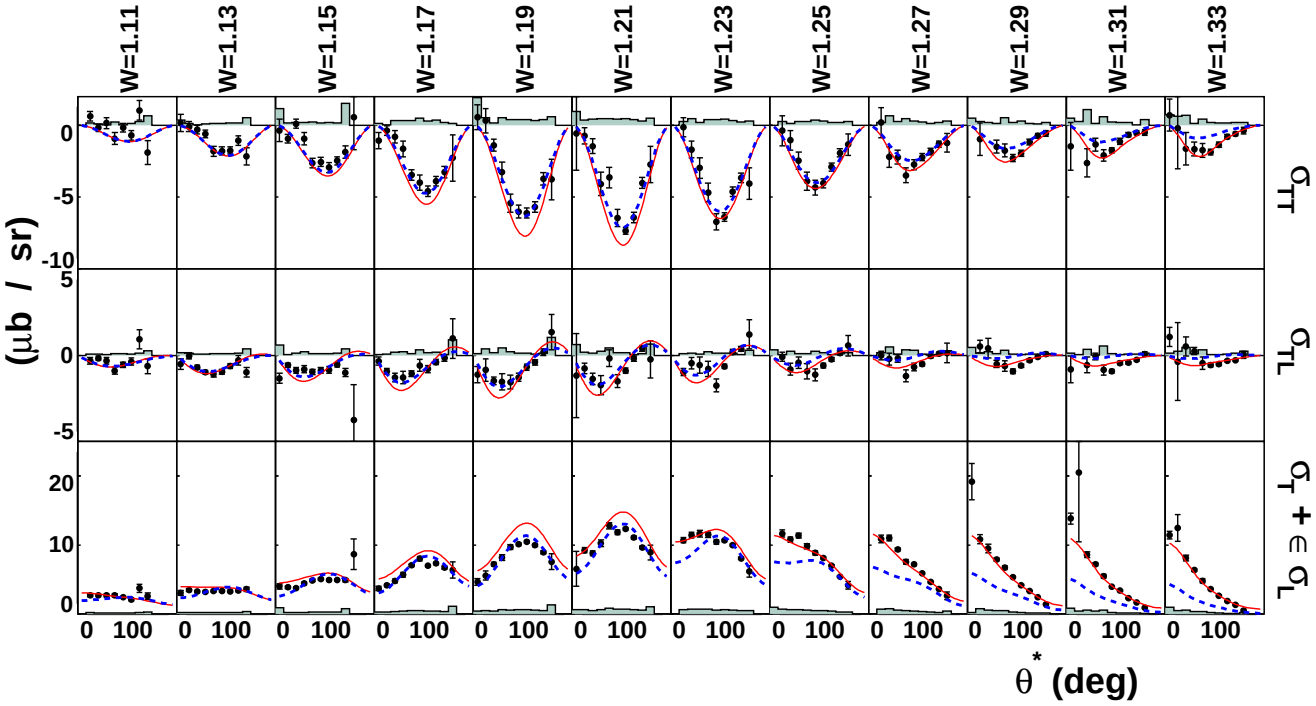

FIG. 23: (Color online) Structure functions versus c.m. θ at $Q^2 = 0.5$ GeV^2. Solid curves represent MAID2003 calculations, while the dashed curves show the predictions of the Sato-Lee model. Shaded areas represent the systematic uncertainties.

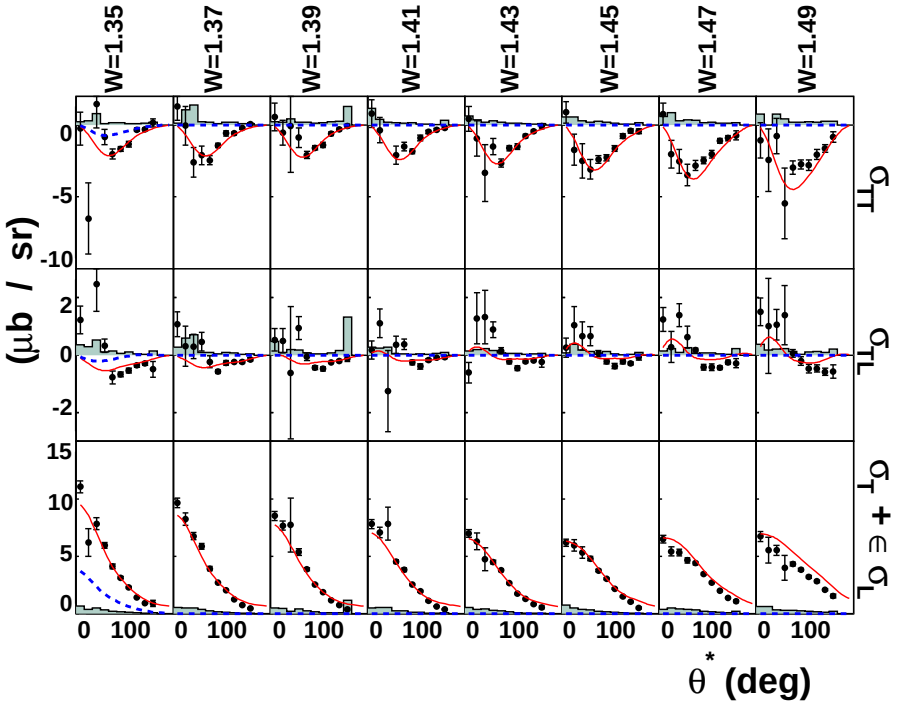

FIG. 24: (Color online) Structure functions versus c.m. θ at $Q^2 = 0.5$ GeV^2. Solid curves represent MAID2003 calculations, while the dashed curves show the predictions of the Sato-Lee model. Shaded areas represent the systematic uncertainties.

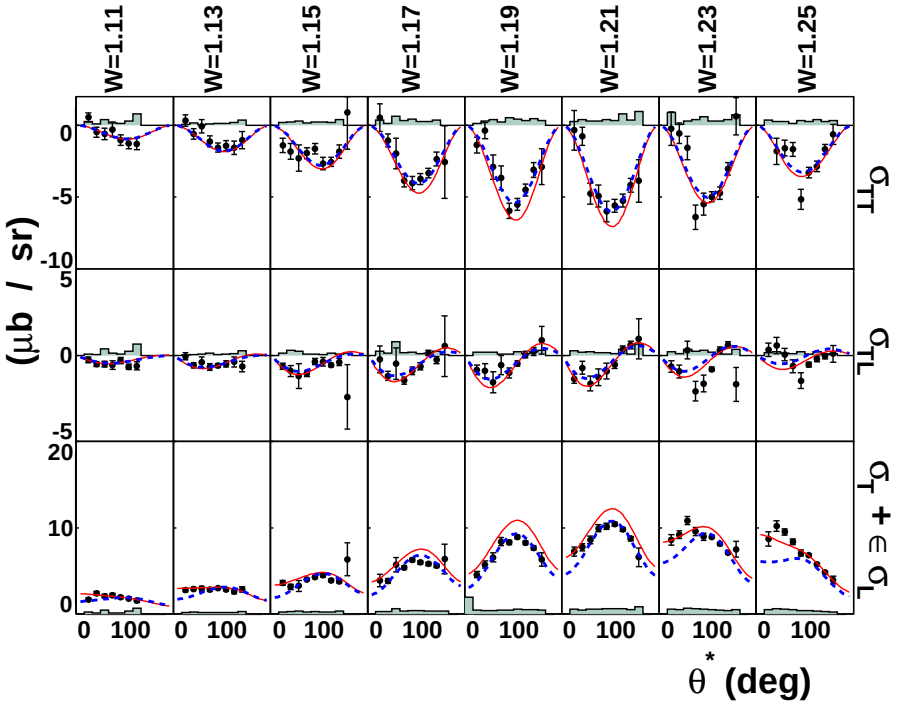

FIG. 25: (Color online) Structure functions versus c.m. θ at $Q^2 = 0.6$ GeV^2. Solid curves represent MAID2003 calculations, while the dashed curves show the predictions of the Sato-Lee model. Shaded areas represent the systematic uncertainties.

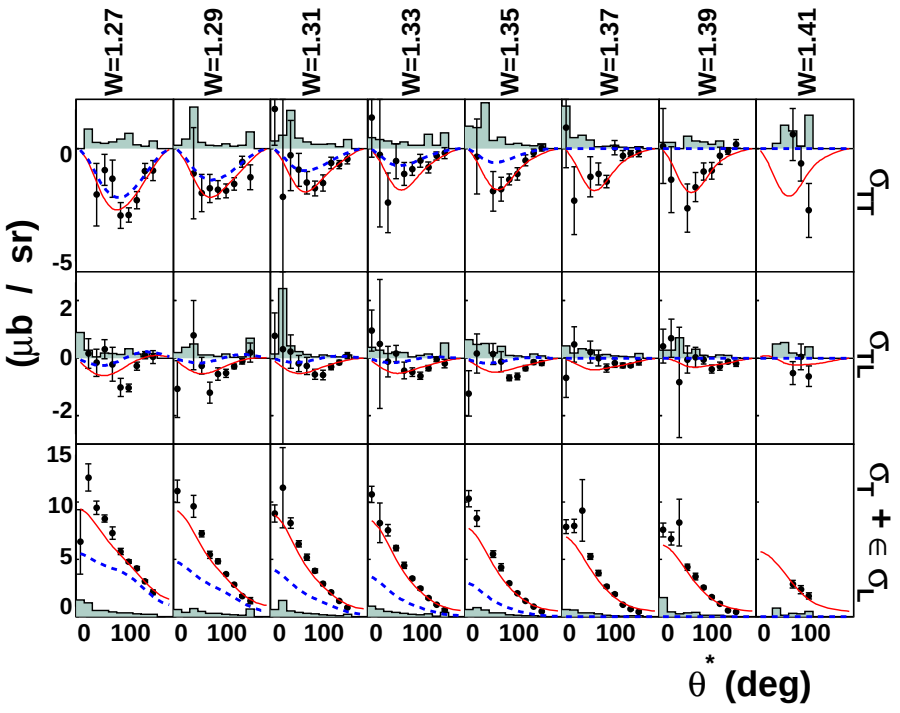

FIG. 26: (Color online) Structure functions versus c.m. θ at $Q^2 = 0.6$ GeV^2. Solid curves represent MAID2003 calculations, while the dashed curves show the predictions of the Sato-Lee model. Shaded areas represent the systematic uncertainties.

APPENDIX B: TABLE OF THE STRUCTURE FUNCTIONS

Q^2	W	ϵ	θ	$\sigma_T + \epsilon\sigma_L$	σ_{TL}	σ_{TT}
0.3	1.11	0.890	7.5	4.396± 0.52	-0.806± 0.34	-0.042± 0.20
0.3	1.11	0.890	22.5	4.243± 0.32	-0.864± 0.18	-0.241± 0.07
0.3	1.11	0.890	37.5	4.285± 0.34	-0.935± 0.15	-0.526± 0.05
0.3	1.11	0.890	52.5	4.580± 0.65	-1.066± 0.43	-0.199± 0.27
0.3	1.11	0.890	67.5	3.556± 0.28	-1.410± 0.20	-1.171± 0.08
0.3	1.11	0.890	82.5	3.673± 0.29	-0.702± 0.19	-0.833± 0.08
0.3	1.11	0.890	97.5	4.121± 0.62	-0.082± 0.57	-0.466± 0.39
0.3	1.11	0.890	112.5	6.547± 1.72	0.693± 1.52	0.658± 1.79
0.3	1.13	0.883	7.5	5.784± 0.56	-0.406± 0.34	-0.404± 0.17
0.3	1.13	0.883	22.5	5.917± 0.41	-1.149± 0.19	-0.110± 0.07
0.3	1.13	0.883	37.5	5.645± 0.61	-1.384± 0.22	-0.922± 0.09
0.3	1.13	0.883	52.5	5.241± 0.40	-1.641± 0.19	-1.427± 0.07
0.3	1.13	0.883	67.5	5.460± 0.37	-1.674± 0.20	-1.951± 0.07
0.3	1.13	0.883	82.5	5.316± 0.38	-1.276± 0.17	-2.225± 0.06
0.3	1.13	0.883	97.5	5.600± 0.55	-0.870± 0.37	-2.175± 0.19
0.3	1.13	0.883	112.5	5.657± 0.52	-1.327± 0.32	-2.496± 0.15
0.3	1.15	0.877	7.5	7.311± 1.18	-0.739± 0.61	-0.551± 0.42
0.3	1.15	0.877	22.5	6.537± 0.45	-1.194± 0.20	-0.158± 0.08
0.3	1.15	0.877	37.5	7.158± 0.63	-1.611± 0.17	-2.997± 0.06
0.3	1.15	0.877	52.5	6.338± 0.44	-2.519± 0.32	-2.156± 0.15
0.3	1.15	0.877	67.5	7.509± 0.48	-2.084± 0.21	-2.558± 0.08
0.3	1.15	0.877	82.5	7.848± 0.66	-1.623± 0.36	-3.256± 0.18
0.3	1.15	0.877	97.5	7.300± 0.56	-1.332± 0.37	-3.871± 0.20
0.3	1.15	0.877	112.5	7.640± 0.53	-0.607± 0.25	-3.243± 0.11
0.3	1.15	0.877	127.5	7.845± 0.73	-0.612± 0.48	-3.815± 0.28
0.3	1.17	0.869	7.5	7.330± 0.58	-0.454± 0.28	-0.207± 0.13
0.3	1.17	0.869	22.5	7.603± 0.57	-1.715± 0.19	-0.908± 0.07
0.3	1.17	0.869	37.5	8.122± 0.62	-2.896± 0.24	-0.985± 0.10
0.3	1.17	0.869	52.5	9.284± 0.59	-3.055± 0.29	-3.644± 0.13
0.3	1.17	0.869	67.5	10.270± 0.65	-2.184± 0.26	-4.977± 0.11
0.3	1.17	0.869	82.5	11.112± 0.79	-1.331± 0.43	-4.833± 0.25
0.3	1.17	0.869	97.5	10.570± 0.69	-1.480± 0.29	-5.635± 0.13
0.3	1.17	0.869	112.5	10.971± 0.71	-0.730± 0.27	-4.924± 0.12
0.3	1.17	0.869	127.5	10.856± 0.91	-1.431± 0.51	-2.195± 0.33
0.3	1.17	0.869	142.5	7.540± 7.69	3.381± 6.69	-6.707±17.31
0.3	1.19	0.861	7.5	10.190± 0.83	0.214± 0.36	1.385± 0.20
0.3	1.19	0.861	22.5	9.489± 0.65	-2.395± 0.24	-0.853± 0.10
0.3	1.19	0.861	37.5	8.671± 2.86	-4.625± 2.39	-3.194± 3.29
0.3	1.19	0.861	52.5	11.957± 0.75	-3.364± 0.37	-5.475± 0.19
0.3	1.19	0.861	67.5	13.780± 0.85	-2.834± 0.28	-6.597± 0.12
0.3	1.19	0.861	82.5	14.775± 0.94	-2.213± 0.40	-7.931± 0.23
0.3	1.19	0.861	97.5	15.489± 0.95	-1.002± 0.23	-7.290± 0.10
0.3	1.19	0.861	112.5	14.238± 0.89	-0.452± 0.30	-6.858± 0.14
0.3	1.19	0.861	127.5	13.144± 0.92	0.281± 0.30	-5.281± 0.15
0.3	1.19	0.861	142.5	15.094± 5.65	-1.826± 4.89	-0.976±10.83
0.3	1.21	0.852	7.5	13.173± 0.90	-0.630± 0.45	0.481± 0.26
0.3	1.21	0.852	22.5	13.751± 1.01	-1.414± 0.49	-0.441± 0.32
0.3	1.21	0.852	37.5	13.970± 1.25	-3.500± 0.45	-3.181± 0.26
0.3	1.21	0.852	52.5	15.069± 1.03	-3.163± 0.54	-6.181± 0.34
0.3	1.21	0.852	67.5	17.425± 1.13	-2.677± 0.45	-7.868± 0.26
0.3	1.21	0.852	82.5	17.842± 1.18	-1.774± 0.52	-10.137± 0.34
0.3	1.21	0.852	97.5	17.510± 1.05	-0.677± 0.25	-8.730± 0.10
0.3	1.21	0.852	112.5	16.208± 0.98	-0.341± 0.17	-8.342± 0.06
0.3	1.21	0.852	127.5	15.215± 1.01	0.015± 0.44	-5.204± 0.28
0.3	1.21	0.852	142.5	16.611± 5.58	-3.116± 4.93	-1.479±10.93
0.3	1.23	0.843	7.5	14.642± 1.22	-1.197± 0.82	1.423± 0.73
0.3	1.23	0.843	22.5	16.339± 1.09	-1.020± 0.41	-1.202± 0.25
0.3	1.23	0.843	37.5	10.757± 1.73	-6.482± 1.53	-7.487± 1.69
0.3	1.23	0.843	52.5	15.822± 1.02	-2.081± 0.53	-5.919± 0.34
0.3	1.23	0.843	67.5	15.578± 1.03	-3.074± 0.60	-9.102± 0.39
0.3	1.23	0.843	82.5	15.771± 0.98	-1.882± 0.40	-9.143± 0.23
0.3	1.23	0.843	97.5	15.657± 0.94	-0.554± 0.19	-8.102± 0.07
0.3	1.23	0.843	112.5	13.738± 0.83	-0.247± 0.16	-6.324± 0.05
0.3	1.23	0.843	127.5	11.743± 0.78	0.303± 0.31	-4.575± 0.15
0.3	1.23	0.843	142.5	11.163± 5.48	-0.964± 4.96	-2.334±11.03
0.3	1.25	0.833	7.5	26.183± 9.95	7.984± 8.65	6.982±25.36
0.3	1.25	0.833	22.5	17.060± 1.08	-0.482± 0.29	-1.241± 0.14
0.3	1.25	0.833	37.5	18.852± 4.32	1.724± 3.68	-0.984± 6.71
0.3	1.25	0.833	52.5	14.817± 1.00	-0.636± 0.55	-4.077± 0.36
0.3	1.25	0.833	67.5	12.789± 0.85	-2.270± 0.42	-7.480± 0.23
0.3	1.25	0.833	82.5	12.440± 0.79	-1.427± 0.28	-6.889± 0.14
0.3	1.25	0.833	97.5	11.586± 0.71	-0.653± 0.15	-5.865± 0.05
0.3	1.25	0.833	112.5	9.878± 0.61	-0.075± 0.14	-4.361± 0.05
0.3	1.25	0.833	127.5	7.996± 0.52	0.190± 0.23	-2.902± 0.11
0.3	1.25	0.833	142.5	4.385± 3.57	2.094± 3.23	-3.533± 5.81
0.3	1.27	0.821	7.5	11.628± 2.07	0.516± 0.72	7.546± 0.55
0.3	1.27	0.821	22.5	15.891± 1.06	0.292± 0.27	0.074± 0.13
0.3	1.27	0.821	37.5	11.540± 5.94	-2.392± 5.08	-4.437±11.43
0.3	1.27	0.821	52.5	12.337± 0.81	-0.700± 0.36	-4.296± 0.21
0.3	1.27	0.821	67.5	10.379± 0.78	-0.954± 0.54	-5.463± 0.39
0.3	1.27	0.821	82.5	9.371± 0.58	-1.127± 0.28	-5.473± 0.13
0.3	1.27	0.821	97.5	7.954± 0.48	-0.509± 0.12	-4.138± 0.04
0.3	1.27	0.821	112.5	6.566± 0.42	-0.418± 0.14	-2.914± 0.04
0.3	1.27	0.821	127.5	4.991± 0.36	0.106± 0.14	-2.405± 0.05
0.3	1.27	0.821	142.5	6.153± 2.12	-2.024± 1.92	0.413± 2.66
0.3	1.29	0.809	7.5	18.693±17.07	-0.955±14.64	-2.284±54.72
0.3	1.29	0.809	22.5	14.630± 1.22	0.020± 0.28	-0.232± 0.13
0.3	1.29	0.809	37.5	10.761± 0.79	-1.691± 0.39	-4.241± 0.22
0.3	1.29	0.809	52.5	10.713± 0.74	-0.022± 0.34	-2.690± 0.17
0.3	1.29	0.809	67.5	8.456± 0.67	-0.940± 0.48	-4.205± 0.31
0.3	1.29	0.809	82.5	7.188± 0.48	-0.537± 0.24	-3.444± 0.11
0.3	1.29	0.809	97.5	5.947± 0.37	-0.632± 0.10	-3.431± 0.03
0.3	1.29	0.809	112.5	4.667± 0.30	-0.481± 0.11	-2.093± 0.03
0.3	1.29	0.809	127.5	3.277± 0.23	-0.185± 0.12	-1.574± 0.04
0.3	1.29	0.809	142.5	2.237± 1.02	0.032± 0.96	-0.966± 0.94
0.3	1.31	0.796	7.5	16.633± 4.46	0.257± 4.10	0.073± 8.28
0.3	1.31	0.796	22.5	14.194± 1.15	1.115± 0.35	0.040± 0.19
0.3	1.31	0.796	37.5	10.545± 0.75	-0.773± 0.36	-3.395± 0.19
0.3	1.31	0.796	52.5	9.837± 0.64	0.306± 0.30	-2.568± 0.14
0.3	1.31	0.796	67.5	6.128± 0.56	-1.904± 0.52	-5.526± 0.33
0.3	1.31	0.796	82.5	5.535± 0.38	-0.760± 0.19	-3.315± 0.08
0.3	1.31	0.796	97.5	4.649± 0.30	-0.693± 0.10	-2.687± 0.02
0.3	1.31	0.796	112.5	3.312± 0.21	-0.323± 0.08	-1.649± 0.02
0.3	1.31	0.796	127.5	2.281± 0.19	-0.220± 0.20	-1.197± 0.08
0.3	1.31	0.796	142.5	1.589± 1.41	-0.109± 1.45	-0.505± 1.58
0.3	1.33	0.782	7.5	22.290± 2.40	-4.533± 1.94	5.550± 2.35
0.3	1.33	0.782	37.5	10.384± 0.83	0.104± 0.41	-3.681± 0.23
0.3	1.33	0.782	52.5	8.508± 0.64	-0.010± 0.27	-3.841± 0.14
0.3	1.33	0.782	67.5	6.063± 0.49	-0.543± 0.33	-3.271± 0.18
0.3	1.33	0.782	82.5	4.680± 0.31	-0.519± 0.15	-2.827± 0.06
0.3	1.33	0.782	97.5	3.584± 0.23	-0.563± 0.08	-2.019± 0.02
0.3	1.33	0.782	112.5	2.611± 0.18	-0.366± 0.08	-1.086± 0.02
0.3	1.33	0.782	127.5	1.536± 0.12	-0.185± 0.07	-0.959± 0.02
0.3	1.33	0.782	142.5	0.625± 1.23	0.286± 1.11	-0.636± 1.03
0.3	1.35	0.767	7.5	16.085± 1.11	-0.229± 0.48	0.125± 0.33
0.3	1.35	0.767	37.5	9.509± 0.81	0.877± 0.47	-1.840± 0.28
0.3	1.35	0.767	52.5	6.997± 0.56	-0.163± 0.18	-3.507± 0.07
0.3	1.35	0.767	67.5	4.947± 0.40	-0.918± 0.23	-4.008± 0.11
0.3	1.35	0.767	82.5	4.056± 0.31	-0.434± 0.14	-2.658± 0.05
0.3	1.35	0.767	97.5	3.038± 0.19	-0.465± 0.06	-1.934± 0.01
0.3	1.35	0.767	112.5	1.982± 0.13	-0.262± 0.05	-0.966± 0.01
0.3	1.35	0.767	127.5	1.163± 0.10	-0.165± 0.07	-0.553± 0.02
0.3	1.35	0.767	142.5	0.238± 1.36	0.527± 1.33	-0.940± 1.38
0.3	1.37	0.751	7.5	14.138± 1.00	0.214± 0.42	0.237± 0.24
0.3	1.37	0.751	22.5	16.143± 3.30	-3.769± 3.59	4.075± 6.77
0.3	1.37	0.751	37.5	8.308± 0.62	1.104± 0.28	-1.647± 0.14
0.3	1.37	0.751	52.5	6.724± 0.56	0.491± 0.26	-2.826± 0.13
0.3	1.37	0.751	67.5	5.199± 0.41	0.112± 0.26	-3.181± 0.12
0.3	1.37	0.751	82.5	3.711± 0.27	-0.197± 0.20	-2.611± 0.08
0.3	1.37	0.751	97.5	2.491± 0.16	-0.415± 0.05	-1.817± 0.01
0.3	1.37	0.751	112.5	1.770± 0.12	-0.304± 0.08	-0.799± 0.02
0.3	1.37	0.751	127.5	1.128± 0.11	-0.250± 0.06	-0.469± 0.01
0.3	1.37	0.751	142.5	1.216± 0.52	-0.617± 0.50	0.209± 0.34
0.3	1.39	0.734	7.5	13.981± 0.91	0.898± 0.50	-0.002± 0.30
0.3	1.39	0.734	37.5	8.470± 0.70	1.782± 0.35	-1.980± 0.18
0.3	1.39	0.734	52.5	6.659± 0.50	0.646± 0.33	-3.588± 0.18
0.3	1.39	0.734	67.5	4.851± 0.48	-0.032± 0.28	-3.155± 0.14
0.3	1.39	0.734	82.5	3.296± 0.23	-0.436± 0.10	-2.655± 0.03
0.3	1.39	0.734	97.5	2.383± 0.15	-0.210± 0.06	-1.684± 0.01
0.3	1.39	0.734	112.5	1.515± 0.11	-0.283± 0.06	-0.810± 0.01
0.3	1.39	0.734	127.5	0.922± 0.08	-0.167± 0.06	-0.559± 0.01
0.3	1.39	0.734	142.5	1.454± 1.47	-0.922± 1.37	0.556± 1.54
0.3	1.41	0.715	7.5	12.408± 0.84	-0.085± 0.32	-1.107± 0.18
0.3	1.41	0.715	22.5	9.119± 1.09	0.371± 0.69	-1.825± 0.56
0.3	1.41	0.715	37.5	7.486± 0.64	1.512± 0.29	-2.465± 0.14
0.3	1.41	0.715	52.5	6.129± 0.44	0.571± 0.33	-3.617± 0.16
0.3	1.41	0.715	67.5	4.480± 0.33	-0.168± 0.20	-3.726± 0.08
0.3	1.41	0.715	82.5	3.244± 0.23	-0.240± 0.11	-2.530± 0.03
0.3	1.41	0.715	97.5	2.297± 0.15	-0.158± 0.05	-1.731± 0.01
0.3	1.41	0.715	112.5	1.425± 0.09	-0.183± 0.04	-1.010± 0.01
0.3	1.41	0.715	127.5	1.015± 0.12	-0.250± 0.09	-0.453± 0.02
0.3	1.41	0.715	142.5	0.785± 0.65	-0.233± 0.46	-0.090± 0.31
0.3	1.43	0.695	7.5	11.388± 0.89	1.796± 0.30	-0.813± 0.15
0.3	1.43	0.695	22.5	7.441± 0.80	0.228± 0.66	-2.310± 0.51
0.3	1.43	0.695	52.5	5.876± 0.59	0.177± 0.35	-4.535± 0.18
0.3	1.43	0.695	67.5	4.644± 0.31	-0.058± 0.11	-3.828± 0.03
0.3	1.43	0.695	82.5	3.518± 0.26	-0.149± 0.19	-2.869± 0.07
0.3	1.43	0.695	97.5	2.345± 0.16	-0.235± 0.05	-1.914± 0.01
0.3	1.43	0.695	112.5	1.574± 0.11	-0.138± 0.04	-1.259± 0.01
0.3	1.43	0.695	127.5	0.980± 0.07	-0.132± 0.05	-0.671± 0.01
0.3	1.43	0.695	142.5	0.856± 0.58	-0.339± 0.58	-0.134± 0.39
0.3	1.45	0.674	7.5	9.761± 0.72	1.533± 0.26	-1.459± 0.12
0.3	1.45	0.674	22.5	6.695± 1.33	0.006± 1.30	-2.646± 1.45
0.3	1.45	0.674	37.5	8.181± 1.35	0.364± 1.01	-2.126± 1.00
0.3	1.45	0.674	52.5	6.718± 0.60	1.298± 0.49	-3.392± 0.31
0.3	1.45	0.674	67.5	4.985± 0.37	-0.037± 0.09	-4.081± 0.02
0.3	1.45	0.674	82.5	3.627± 0.26	-0.158± 0.10	-2.970± 0.03
0.3	1.45	0.674	97.5	2.730± 0.19	-0.212± 0.05	-2.476± 0.01
0.3	1.45	0.674	112.5	1.883± 0.13	-0.207± 0.04	-1.507± 0.01
0.3	1.45	0.674	127.5	1.269± 0.09	-0.209± 0.05	-0.806± 0.01
0.3	1.45	0.674	142.5	1.520± 1.20	-0.751± 1.20	0.099± 1.11
0.3	1.47	0.652	7.5	10.384± 0.71	1.601± 0.30	-0.872± 0.15
0.3	1.47	0.652	22.5	8.966± 1.90	2.585± 1.97	-0.794± 2.77
0.3	1.47	0.652	37.5	7.325± 0.55	1.430± 0.40	-3.595± 0.23
0.3	1.47	0.652	52.5	6.294± 0.47	0.016± 0.34	-5.393± 0.17
0.3	1.47	0.652	67.5	5.710± 0.39	0.058± 0.11	-4.814± 0.03
0.3	1.47	0.652	82.5	4.442± 0.34	0.016± 0.23	-3.808± 0.10
0.3	1.47	0.652	97.5	3.550± 0.23	-0.262± 0.07	-2.739± 0.02
0.3	1.47	0.652	112.5	2.577± 0.17	-0.307± 0.07	-1.997± 0.01
0.3	1.47	0.652	127.5	1.916± 0.14	-0.215± 0.06	-1.358± 0.01
0.3	1.47	0.652	142.5	1.586± 0.67	-0.471± 0.80	-0.438± 0.61
0.3	1.49	0.628	7.5	10.202± 0.70	1.896± 0.37	0.293± 0.19
0.3	1.49	0.628	22.5	6.937± 1.34	0.655± 1.26	-2.310± 1.35
0.3	1.49	0.628	52.5	6.063± 0.44	-0.040± 0.35	-4.892± 0.19
0.3	1.49	0.628	67.5	5.706± 0.42	0.085± 0.14	-4.624± 0.04
0.3	1.49	0.628	82.5	4.947± 0.36	-0.101± 0.20	-4.544± 0.09
0.3	1.49	0.628	97.5	4.199± 0.29	-0.354± 0.07	-3.412± 0.02
0.3	1.49	0.628	112.5	3.542± 0.25	-0.387± 0.06	-3.278± 0.01
0.3	1.49	0.628	127.5	2.678± 0.20	-0.392± 0.10	-2.050± 0.03
0.3	1.49	0.628	142.5	2.122± 0.35	-0.400± 0.40	-1.334± 0.21
0.3	1.51	0.602	7.5	11.363± 0.81	1.969± 0.46	0.260± 0.27
0.3	1.51	0.602	22.5	8.248± 1.51	1.289± 1.59	-1.480± 1.98
0.3	1.51	0.602	37.5	7.380± 1.11	1.315± 0.78	-2.254± 0.67
0.3	1.51	0.602	52.5	5.285± 0.41	0.255± 0.39	-3.690± 0.23
0.3	1.51	0.602	67.5	4.250± 0.27	-0.111± 0.08	-3.596± 0.02
0.3	1.51	0.602	82.5	3.825± 0.30	-0.230± 0.19	-3.628± 0.07
0.3	1.51	0.602	97.5	3.590± 0.24	-0.353± 0.06	-3.310± 0.01
0.3	1.51	0.602	112.5	3.379± 0.23	-0.294± 0.07	-2.952± 0.02
0.3	1.51	0.602	127.5	2.683± 0.20	-0.263± 0.08	-1.985± 0.02
0.3	1.51	0.602	142.5	2.002± 0.53	0.042± 0.62	-1.599± 0.48
0.3	1.53	0.575	7.5	13.190± 1.08	2.641± 0.65	1.165± 0.47
0.3	1.53	0.575	22.5	5.607± 1.20	-2.410± 1.61	-5.446± 1.84
0.3	1.53	0.575	37.5	6.150± 0.57	0.443± 0.57	-1.619± 0.40
0.3	1.53	0.575	67.5	2.767± 0.18	-0.088± 0.10	-1.846± 0.03
0.3	1.53	0.575	82.5	2.494± 0.19	-0.103± 0.12	-2.088± 0.04
0.3	1.53	0.575	97.5	2.621± 0.16	-0.178± 0.06	-2.316± 0.01
0.3	1.53	0.575	112.5	2.732± 0.18	-0.043± 0.06	-2.315± 0.01
0.3	1.53	0.575	127.5	2.528± 0.17	-0.104± 0.09	-1.536± 0.03
0.3	1.53	0.575	142.5	2.217± 0.36	-0.119± 0.35	-1.366± 0.18
0.3	1.55	0.547	7.5	14.342± 1.48	3.682± 1.43	-0.848± 1.47
0.3	1.55	0.547	22.5	8.640± 1.77	1.923± 1.77	-0.618± 2.23

Q^2	W	ϵ	θ	$\sigma_T + \epsilon\sigma_L$	σ_{TL}	σ_{TT}
0.3	1.55	0.547	37.5	4.925± 0.47	0.071± 0.54	-2.457± 0.36
0.3	1.55	0.547	52.5	2.717± 0.62	0.070± 0.59	-2.645± 0.45
0.3	1.55	0.547	67.5	1.893± 0.13	-0.171± 0.08	-1.520± 0.02
0.3	1.55	0.547	82.5	1.433± 0.14	-0.117± 0.12	-1.254± 0.04
0.3	1.55	0.547	97.5	1.620± 0.11	0.009± 0.05	-1.227± 0.01
0.3	1.55	0.547	112.5	1.929± 0.14	0.006± 0.05	-1.558± 0.01
0.3	1.55	0.547	127.5	1.872± 0.14	0.045± 0.06	-1.166± 0.01
0.3	1.55	0.547	142.5	1.628± 0.21	0.095± 0.13	-0.840± 0.04
0.3	1.57	0.516	7.5	11.843± 2.00	1.512± 2.37	1.356± 3.65
0.3	1.57	0.516	22.5	7.309± 1.78	0.685± 2.31	-2.492± 3.51
0.3	1.57	0.516	37.5	3.701± 0.41	-0.790± 0.53	-3.581± 0.37
0.3	1.57	0.516	52.5	2.138± 0.44	0.070± 0.44	-3.372± 0.29
0.3	1.57	0.516	67.5	1.460± 0.12	-0.207± 0.11	-0.869± 0.03
0.3	1.57	0.516	82.5	0.992± 0.11	-0.041± 0.12	-0.346± 0.04
0.3	1.57	0.516	97.5	1.036± 0.08	0.000± 0.09	-0.575± 0.02
0.3	1.57	0.516	112.5	1.491± 0.14	0.111± 0.06	-0.992± 0.01
0.3	1.57	0.516	127.5	1.492± 0.11	0.148± 0.09	-0.626± 0.02
0.3	1.57	0.516	142.5	1.293± 0.16	0.401± 0.17	-0.876± 0.07
0.4	1.11	0.850	7.5	3.026± 0.56	-0.592± 0.44	1.302± 0.25
0.4	1.11	0.850	22.5	3.448± 0.27	-0.265± 0.14	-0.159± 0.05
0.4	1.11	0.850	37.5	3.315± 0.27	-0.698± 0.14	-0.057± 0.05
0.4	1.11	0.850	52.5	3.303± 0.32	-1.003± 0.23	-0.247± 0.10
0.4	1.11	0.850	67.5	2.823± 0.27	-1.005± 0.24	-1.012± 0.10
0.4	1.11	0.850	82.5	3.131± 0.24	-0.668± 0.16	-0.816± 0.06
0.4	1.11	0.850	97.5	3.014± 0.34	-0.692± 0.27	-0.961± 0.12
0.4	1.11	0.850	112.5	3.226± 1.19	-0.409± 1.17	-0.380± 1.21
0.4	1.13	0.843	7.5	5.045± 0.66	-0.204± 0.35	-0.503± 0.18
0.4	1.13	0.843	22.5	4.058± 0.30	-0.729± 0.14	-0.247± 0.05
0.4	1.13	0.843	37.5	4.385± 0.32	-0.992± 0.16	-0.106± 0.06
0.4	1.13	0.843	52.5	4.441± 0.42	-0.994± 0.21	-1.153± 0.08
0.4	1.13	0.843	67.5	4.314± 0.30	-0.990± 0.15	-1.460± 0.05
0.4	1.13	0.843	82.5	4.453± 0.31	-1.035± 0.15	-1.705± 0.05
0.4	1.13	0.843	97.5	4.093± 0.34	-1.080± 0.26	-2.391± 0.11
0.4	1.13	0.843	112.5	4.252± 0.33	-0.961± 0.19	-1.547± 0.08
0.4	1.13	0.843	127.5	4.292± 0.42	0.021± 0.27	-3.695± 0.12
0.4	1.15	0.834	7.5	4.608± 0.44	-0.048± 0.24	0.481± 0.11
0.4	1.15	0.834	22.5	4.839± 0.33	-0.842± 0.14	-0.648± 0.05
0.4	1.15	0.834	37.5	5.180± 0.38	-1.272± 0.14	-1.102± 0.05
0.4	1.15	0.834	52.5	5.254± 0.38	-1.879± 0.22	-1.928± 0.09
0.4	1.15	0.834	67.5	6.121± 0.39	-1.328± 0.18	-2.266± 0.06
0.4	1.15	0.834	82.5	6.501± 0.44	-1.051± 0.22	-2.676± 0.09
0.4	1.15	0.834	97.5	6.084± 0.46	-1.073± 0.24	-3.514± 0.11
0.4	1.15	0.834	112.5	6.052± 0.41	-0.554± 0.18	-2.880± 0.06
0.4	1.15	0.834	127.5	6.371± 0.59	-0.344± 0.44	-2.613± 0.25
0.4	1.15	0.834	142.5	7.645± 2.36	-1.068± 2.05	-0.795± 2.94
0.4	1.17	0.826	7.5	5.183± 0.49	-0.969± 0.26	0.026± 0.12
0.4	1.17	0.826	22.5	5.743± 0.39	-1.429± 0.16	-0.870± 0.05
0.4	1.17	0.826	37.5	6.654± 0.66	-1.252± 0.45	-0.340± 0.29
0.4	1.17	0.826	52.5	7.210± 0.46	-2.289± 0.23	-3.481± 0.10
0.4	1.17	0.826	67.5	8.043± 0.52	-1.466± 0.23	-3.867± 0.10
0.4	1.17	0.826	82.5	8.874± 0.61	-1.391± 0.27	-4.932± 0.12
0.4	1.17	0.826	97.5	8.568± 0.58	-1.323± 0.25	-5.178± 0.11
0.4	1.17	0.826	112.5	8.755± 0.55	-0.646± 0.15	-4.590± 0.05
0.4	1.17	0.826	127.5	8.386± 0.60	-0.424± 0.40	-2.863± 0.21
0.4	1.17	0.826	142.5	6.490± 2.24	3.447± 2.60	-5.914± 3.53
0.4	1.19	0.816	7.5	7.686± 0.64	-0.368± 0.24	-0.778± 0.11
0.4	1.19	0.816	22.5	7.180± 0.58	-2.041± 0.29	-2.011± 0.14
0.4	1.19	0.816	37.5	8.637± 0.61	-1.994± 0.33	-2.056± 0.16
0.4	1.19	0.816	52.5	9.435± 0.69	-2.779± 0.49	-4.851± 0.29
0.4	1.19	0.816	67.5	11.654± 0.74	-2.144± 0.31	-6.047± 0.15
0.4	1.19	0.816	82.5	12.359± 0.79	-1.784± 0.34	-7.104± 0.17
0.4	1.19	0.816	97.5	12.523± 0.76	-0.764± 0.16	-6.557± 0.06
0.4	1.19	0.816	112.5	12.034± 0.74	-0.268± 0.19	-5.973± 0.07
0.4	1.19	0.816	127.5	11.437± 0.74	-0.509± 0.32	-3.368± 0.16
0.4	1.19	0.816	142.5	6.464± 1.96	4.437± 1.80	-8.293± 2.42
0.4	1.21	0.806	7.5	10.629± 0.97	-1.161± 0.66	-1.591± 0.52
0.4	1.21	0.806	22.5	10.347± 0.72	-1.708± 0.33	-0.492± 0.16
0.4	1.21	0.806	37.5	11.336± 0.92	-2.215± 0.41	-2.583± 0.22
0.4	1.21	0.806	52.5	13.319± 1.05	-1.537± 0.76	-4.211± 0.61
0.4	1.21	0.806	67.5	14.824± 0.99	-1.601± 0.50	-7.055± 0.33
0.4	1.21	0.806	82.5	14.388± 0.95	-2.225± 0.36	-9.401± 0.19
0.4	1.21	0.806	97.5	15.504± 0.93	-0.987± 0.23	-8.303± 0.10
0.4	1.21	0.806	112.5	13.911± 0.85	-0.142± 0.16	-7.085± 0.07
0.4	1.21	0.806	127.5	12.328± 0.79	0.116± 0.27	-5.073± 0.13
0.4	1.21	0.806	142.5	12.066± 1.95	-0.743± 1.63	-1.899± 1.94
0.4	1.23	0.795	7.5	11.708± 3.72	-0.856± 3.40	-1.593± 6.26
0.4	1.23	0.795	22.5	13.914± 1.04	-0.465± 0.32	-1.624± 0.16
0.4	1.23	0.795	37.5	12.940± 0.90	-1.533± 0.39	-3.270± 0.22
0.4	1.23	0.795	52.5	13.269± 0.87	-1.966± 0.47	-4.924± 0.30
0.4	1.23	0.795	67.5	14.214± 0.91	-1.158± 0.37	-5.951± 0.21
0.4	1.23	0.795	82.5	13.309± 0.86	-1.329± 0.43	-7.421± 0.23
0.4	1.23	0.795	97.5	13.116± 0.79	-0.789± 0.21	-7.061± 0.08
0.4	1.23	0.795	112.5	11.843± 0.71	-0.130± 0.15	-5.314± 0.06
0.4	1.23	0.795	127.5	9.943± 0.61	0.488± 0.19	-3.987± 0.08
0.4	1.23	0.795	142.5	8.864± 1.56	-0.666± 1.40	-0.921± 1.41
0.4	1.25	0.783	22.5	13.387± 0.91	-0.006± 0.29	-0.282± 0.14
0.4	1.25	0.783	37.5	12.410± 0.95	-0.725± 0.52	-1.046± 0.36
0.4	1.25	0.783	52.5	12.555± 0.86	-0.551± 0.44	-3.525± 0.29
0.4	1.25	0.783	67.5	11.558± 0.79	-0.931± 0.42	-4.732± 0.26
0.4	1.25	0.783	82.5	10.427± 0.69	-1.245± 0.30	-5.298± 0.15
0.4	1.25	0.783	97.5	9.799± 0.60	-0.698± 0.16	-5.462± 0.05
0.4	1.25	0.783	112.5	8.530± 0.53	-0.211± 0.12	-4.097± 0.04
0.4	1.25	0.783	127.5	6.740± 0.46	0.244± 0.17	-2.504± 0.06
0.4	1.25	0.783	142.5	4.298± 1.06	0.813± 0.95	-2.804± 0.84
0.4	1.27	0.770	22.5	13.365± 0.94	0.430± 0.29	1.435± 0.15
0.4	1.27	0.770	37.5	12.235± 1.03	-0.357± 0.53	-2.254± 0.34
0.4	1.27	0.770	52.5	11.206± 0.75	-0.323± 0.32	-2.769± 0.17
0.4	1.27	0.770	67.5	9.097± 0.63	-1.080± 0.38	-4.248± 0.22
0.4	1.27	0.770	82.5	8.357± 0.54	-0.789± 0.24	-4.072± 0.11
0.4	1.27	0.770	97.5	7.057± 0.45	-0.654± 0.16	-3.561± 0.05
0.4	1.27	0.770	112.5	5.728± 0.35	-0.335± 0.10	-2.374± 0.03
0.4	1.27	0.770	127.5	4.406± 0.38	-0.137± 0.26	-2.038± 0.12
0.4	1.27	0.770	142.5	3.406± 1.13	-0.057± 1.04	-1.007± 0.90
0.4	1.29	0.757	7.5	20.088±10.46	-4.928± 9.92	5.324±31.23
0.4	1.29	0.757	22.5	13.465± 1.08	0.290± 0.29	-2.148± 0.14
0.4	1.29	0.757	37.5	10.746± 0.89	-0.167± 0.55	-1.414± 0.35
0.4	1.29	0.757	52.5	9.464± 0.61	0.001± 0.18	-2.089± 0.07
0.4	1.29	0.757	67.5	7.110± 0.55	-1.180± 0.38	-3.252± 0.20
0.4	1.29	0.757	82.5	6.630± 0.41	-0.729± 0.13	-2.639± 0.04
0.4	1.29	0.757	97.5	5.024± 0.33	-0.653± 0.18	-2.176± 0.06
0.4	1.29	0.757	112.5	3.862± 0.24	-0.390± 0.09	-1.519± 0.02
0.4	1.29	0.757	127.5	2.770± 0.20	-0.207± 0.08	-1.215± 0.02
0.4	1.29	0.757	142.5	1.998± 0.81	-0.212± 0.79	-0.727± 0.65
0.4	1.31	0.742	7.5	16.645± 2.87	-2.076± 2.94	1.145± 4.34
0.4	1.31	0.742	22.5	13.185± 1.23	-0.187± 0.52	-1.300± 0.36
0.4	1.31	0.742	37.5	9.716± 1.14	-0.207± 0.94	-2.259± 0.79
0.4	1.31	0.742	52.5	8.482± 0.57	-0.116± 0.23	-2.050± 0.10
0.4	1.31	0.742	67.5	5.575± 0.44	-1.115± 0.33	-3.102± 0.18
0.4	1.31	0.742	82.5	4.906± 0.32	-0.621± 0.17	-2.543± 0.06
0.4	1.31	0.742	97.5	4.012± 0.27	-0.468± 0.12	-1.918± 0.03
0.4	1.31	0.742	112.5	2.746± 0.18	-0.414± 0.08	-1.062± 0.02
0.4	1.31	0.742	127.5	1.790± 0.13	-0.155± 0.06	-0.999± 0.01
0.4	1.31	0.742	142.5	1.005± 0.34	0.292± 0.35	-0.540± 0.19
0.4	1.33	0.726	7.5	14.481± 1.03	-0.836± 0.62	-0.892± 0.45
0.4	1.33	0.726	22.5	12.583± 2.70	-0.580± 2.78	-1.031± 4.61
0.4	1.33	0.726	37.5	9.506± 0.72	0.043± 0.42	-2.850± 0.26
0.4	1.33	0.726	52.5	7.160± 0.48	-0.226± 0.20	-2.266± 0.08
0.4	1.33	0.726	67.5	4.769± 0.37	-1.118± 0.24	-2.891± 0.11
0.4	1.33	0.726	82.5	4.537± 0.32	-0.250± 0.18	-1.643± 0.07
0.4	1.33	0.726	97.5	3.176± 0.20	-0.669± 0.09	-1.843± 0.02
0.4	1.33	0.726	112.5	2.301± 0.15	-0.519± 0.07	-1.041± 0.02
0.4	1.33	0.726	127.5	1.401± 0.15	-0.283± 0.10	-0.669± 0.03
0.4	1.33	0.726	142.5	1.480± 1.07	-0.816± 1.06	0.269± 1.03
0.4	1.35	0.709	7.5	12.538± 0.87	0.038± 0.38	-0.776± 0.23
0.4	1.35	0.709	22.5	12.641± 1.70	-0.736± 1.81	1.983± 2.41
0.4	1.35	0.709	37.5	8.794± 0.63	1.050± 0.44	-1.406± 0.26
0.4	1.35	0.709	52.5	6.262± 0.47	-0.205± 0.18	-2.630± 0.07
0.4	1.35	0.709	67.5	5.251± 0.42	0.126± 0.28	-2.136± 0.15
0.4	1.35	0.709	82.5	3.660± 0.26	-0.361± 0.17	-1.911± 0.06
0.4	1.35	0.709	97.5	2.649± 0.17	-0.504± 0.07	-1.500± 0.02
0.4	1.35	0.709	112.5	1.839± 0.12	-0.371± 0.05	-0.878± 0.01
0.4	1.35	0.709	127.5	1.093± 0.11	-0.294± 0.10	-0.411± 0.03
0.4	1.35	0.709	142.5	0.923± 0.29	-0.366± 0.28	-0.064± 0.14
0.4	1.37	0.691	7.5	10.500± 0.75	-0.023± 0.30	-0.477± 0.16
0.4	1.37	0.691	22.5	10.651± 1.23	0.178± 1.28	0.962± 1.40
0.4	1.37	0.691	37.5	7.576± 0.55	0.992± 0.38	-1.692± 0.22
0.4	1.37	0.691	52.5	6.200± 0.48	0.363± 0.28	-2.621± 0.12
0.4	1.37	0.691	67.5	4.303± 0.38	-0.423± 0.22	-2.805± 0.09
0.4	1.37	0.691	82.5	3.357± 0.22	-0.345± 0.11	-2.107± 0.03
0.4	1.37	0.691	97.5	2.200± 0.15	-0.423± 0.07	-1.432± 0.02
0.4	1.37	0.691	112.5	1.392± 0.09	-0.212± 0.06	-0.803± 0.01
0.4	1.37	0.691	127.5	0.919± 0.08	-0.240± 0.05	-0.404± 0.01
0.4	1.37	0.691	142.5	0.607± 0.21	-0.129± 0.21	-0.213± 0.08
0.4	1.39	0.672	7.5	10.145± 0.72	0.725± 0.33	-1.417± 0.17
0.4	1.39	0.672	22.5	8.519± 0.87	0.344± 0.56	-1.264± 0.37
0.4	1.39	0.672	37.5	6.839± 0.57	1.172± 0.43	-1.647± 0.24
0.4	1.39	0.672	52.5	5.273± 0.40	0.282± 0.22	-2.464± 0.10
0.4	1.39	0.672	67.5	4.353± 0.39	-0.104± 0.21	-2.589± 0.09
0.4	1.39	0.672	82.5	2.844± 0.19	-0.323± 0.10	-2.192± 0.03
0.4	1.39	0.672	97.5	2.062± 0.16	-0.303± 0.07	-1.166± 0.02
0.4	1.39	0.672	112.5	1.327± 0.09	-0.244± 0.04	-0.817± 0.01
0.4	1.39	0.672	127.5	0.841± 0.10	-0.191± 0.04	-0.397± 0.01
0.4	1.39	0.672	142.5	0.478± 0.33	-0.100± 0.34	-0.119± 0.18
0.4	1.41	0.652	7.5	9.513± 0.75	0.998± 0.30	-0.006± 0.16
0.4	1.41	0.652	22.5	7.418± 0.58	0.733± 0.40	-1.663± 0.22
0.4	1.41	0.652	37.5	7.764± 1.57	-0.336± 1.38	0.322± 1.61
0.4	1.41	0.652	52.5	5.225± 0.39	0.312± 0.25	-3.468± 0.12
0.4	1.41	0.652	67.5	4.122± 0.29	0.035± 0.11	-2.973± 0.03
0.4	1.41	0.652	82.5	2.937± 0.20	-0.301± 0.08	-1.971± 0.02
0.4	1.41	0.652	97.5	2.051± 0.14	-0.228± 0.07	-1.168± 0.02
0.4	1.41	0.652	112.5	1.245± 0.12	-0.270± 0.07	-0.683± 0.02
0.4	1.41	0.652	127.5	0.776± 0.06	-0.167± 0.03	-0.456± 0.01
0.4	1.41	0.652	142.5	0.699± 0.21	-0.353± 0.21	0.051± 0.09
0.4	1.43	0.630	7.5	8.054± 0.82	0.720± 0.30	0.173± 0.14
0.4	1.43	0.630	22.5	7.594± 0.71	1.440± 0.64	-0.764± 0.46
0.4	1.43	0.630	37.5	5.185± 1.39	2.236± 1.29	-3.661± 1.44
0.4	1.43	0.630	52.5	5.248± 0.51	0.577± 0.35	-2.945± 0.17
0.4	1.43	0.630	67.5	4.362± 0.29	0.078± 0.11	-3.157± 0.03
0.4	1.43	0.630	82.5	2.839± 0.19	-0.379± 0.07	-2.452± 0.02
0.4	1.43	0.630	97.5	2.128± 0.15	-0.313± 0.07	-1.625± 0.02
0.4	1.43	0.630	112.5	1.394± 0.10	-0.224± 0.06	-0.882± 0.01
0.4	1.43	0.630	127.5	0.922± 0.08	-0.171± 0.05	-0.366± 0.01
0.4	1.43	0.630	142.5	0.681± 0.21	-0.258± 0.25	-0.101± 0.11
0.4	1.45	0.607	7.5	7.515± 0.59	0.441± 0.29	-0.007± 0.13
0.4	1.45	0.607	22.5	7.144± 0.92	1.425± 0.83	-1.704± 0.64
0.4	1.45	0.607	37.5	7.303± 0.72	0.507± 0.55	-1.910± 0.36
0.4	1.45	0.607	52.5	4.973± 0.40	-0.047± 0.24	-4.138± 0.11
0.4	1.45	0.607	67.5	4.293± 0.32	0.097± 0.11	-3.189± 0.04
0.4	1.45	0.607	82.5	3.317± 0.23	-0.301± 0.09	-2.808± 0.02
0.4	1.45	0.607	97.5	2.377± 0.18	-0.281± 0.10	-1.857± 0.02
0.4	1.45	0.607	112.5	1.661± 0.12	-0.265± 0.06	-1.127± 0.01
0.4	1.45	0.607	127.5	1.140± 0.08	-0.213± 0.05	-0.786± 0.01
0.4	1.45	0.607	142.5	0.718± 0.08	-0.097± 0.08	-0.624± 0.02
0.4	1.47	0.582	7.5	7.799± 0.58	0.462± 0.25	-0.124± 0.12
0.4	1.47	0.582	22.5	7.598± 1.02	2.182± 0.89	-0.943± 0.73
0.4	1.47	0.582	37.5	6.561± 0.64	1.589± 0.43	-2.271± 0.26
0.4	1.47	0.582	52.5	5.648± 0.40	0.341± 0.38	-4.398± 0.23
0.4	1.47	0.582	67.5	4.635± 0.33	0.008± 0.12	-3.282± 0.04
0.4	1.47	0.582	82.5	3.632± 0.29	-0.479± 0.08	-3.444± 0.02
0.4	1.47	0.582	97.5	3.079± 0.21	-0.462± 0.10	-2.236± 0.03
0.4	1.47	0.582	112.5	2.338± 0.17	-0.377± 0.05	-1.632± 0.01
0.4	1.47	0.582	127.5	1.668± 0.12	-0.373± 0.06	-1.076± 0.01
0.4	1.47	0.582	142.5	1.039± 0.33	-0.154± 0.33	-0.632± 0.18
0.4	1.49	0.557	7.5	8.104± 0.88	0.964± 0.29	0.314± 0.15
0.4	1.49	0.557	22.5	5.764± 1.00	0.100± 1.08	-3.494± 1.09
0.4	1.49	0.557	37.5	6.555± 1.04	1.148± 1.01	-2.172± 0.88
0.4	1.49	0.557	52.5	5.826± 0.40	0.497± 0.37	-4.188± 0.21
0.4	1.49	0.557	67.5	5.013± 0.37	0.170± 0.14	-4.030± 0.04
0.4	1.49	0.557	82.5	4.242± 0.30	-0.380± 0.12	-3.697± 0.04
0.4	1.49	0.557	97.5	3.545± 0.25	-0.422± 0.09	-2.900± 0.02
0.4	1.49	0.557	112.5	3.114± 0.24	-0.541± 0.08	-2.456± 0.02
0.4	1.49	0.557	127.5	2.446± 0.17	-0.339± 0.13	-1.694± 0.04
0.4	1.49	0.557	142.5	1.685± 0.19	-0.357± 0.19	-0.875± 0.07
0.4	1.51	0.529	7.5	9.273± 0.67	1.069± 0.43	0.303± 0.24
0.4	1.51	0.529	22.5	7.981± 1.79	2.924± 1.98	-0.555± 2.77
0.4	1.51	0.529	37.5	5.743± 0.57	0.985± 0.55	-1.511± 0.39

Q^2	W	ϵ	θ	$\sigma_T + \epsilon\sigma_L$	σ_{TL}	σ_{TT}
0.4	1.51	0.529	67.5	3.641± 0.25	0.185± 0.10	-2.581± 0.03
0.4	1.51	0.529	82.5	3.220± 0.21	-0.331± 0.09	-3.287± 0.03
0.4	1.51	0.529	97.5	3.228± 0.22	-0.193± 0.13	-2.325± 0.04
0.4	1.51	0.529	112.5	2.926± 0.22	-0.331± 0.06	-2.279± 0.01
0.4	1.51	0.529	127.5	2.497± 0.17	-0.360± 0.08	-1.452± 0.02
0.4	1.51	0.529	142.5	1.833± 0.28	-0.408± 0.20	-1.176± 0.07
0.4	1.53	0.501	7.5	11.265± 0.91	1.667± 0.75	1.800± 0.59
0.4	1.53	0.501	22.5	7.033± 1.59	0.924± 1.80	-1.253± 2.42
0.4	1.53	0.501	37.5	4.894± 0.50	0.400± 0.60	-1.814± 0.42
0.4	1.53	0.501	52.5	4.648± 0.73	-1.267± 0.71	0.770± 0.59
0.4	1.53	0.501	67.5	2.452± 0.19	0.118± 0.08	-1.947± 0.02
0.4	1.53	0.501	82.5	2.171± 0.15	-0.078± 0.09	-1.888± 0.03
0.4	1.53	0.501	97.5	2.356± 0.20	-0.318± 0.11	-2.149± 0.03
0.4	1.53	0.501	112.5	2.486± 0.17	-0.289± 0.11	-2.218± 0.03
0.4	1.53	0.501	127.5	2.140± 0.16	-0.167± 0.08	-1.534± 0.02
0.4	1.53	0.501	142.5	1.759± 0.20	-0.260± 0.17	-0.697± 0.06
0.4	1.55	0.470	97.5	1.236± 0.23	0.242± 0.26	-1.528± 0.13
0.5	1.11	0.808	22.5	2.702± 0.33	-0.322± 0.20	0.624± 0.08
0.5	1.11	0.808	37.5	2.709± 0.25	-0.169± 0.13	-0.182± 0.04
0.5	1.11	0.808	52.5	2.718± 0.30	-0.316± 0.21	0.161± 0.09
0.5	1.11	0.808	67.5	2.726± 0.26	-0.892± 0.23	-0.922± 0.10
0.5	1.11	0.808	82.5	2.462± 0.21	-0.551± 0.19	-0.173± 0.07
0.5	1.11	0.808	97.5	2.104± 0.24	-0.360± 0.21	-0.695± 0.09
0.5	1.11	0.808	112.5	3.745± 0.64	0.926± 0.58	1.033± 0.42
0.5	1.11	0.808	127.5	2.589± 0.58	-0.631± 0.51	-1.897± 0.32
0.5	1.13	0.799	7.5	3.062± 0.44	-0.520± 0.34	0.161± 0.18
0.5	1.13	0.799	22.5	3.523± 0.33	-0.028± 0.23	-0.095± 0.09
0.5	1.13	0.799	37.5	3.282± 0.29	-0.697± 0.14	-0.308± 0.05
0.5	1.13	0.799	52.5	3.233± 0.28	-0.972± 0.13	-0.608± 0.04
0.5	1.13	0.799	67.5	3.368± 0.25	-1.096± 0.18	-1.802± 0.06
0.5	1.13	0.799	82.5	3.362± 0.24	-0.960± 0.17	-1.786± 0.06
0.5	1.13	0.799	97.5	3.301± 0.31	-0.615± 0.17	-1.752± 0.06
0.5	1.13	0.799	112.5	3.446± 0.36	-0.290± 0.30	-1.080± 0.15
0.5	1.13	0.799	127.5	3.622± 0.52	-0.989± 0.47	-2.179± 0.28
0.5	1.15	0.789	7.5	4.027± 0.98	-1.328± 0.66	-0.354± 0.48
0.5	1.15	0.789	22.5	3.890± 0.31	-0.573± 0.13	-0.941± 0.04
0.5	1.15	0.789	37.5	3.803± 0.30	-0.864± 0.21	0.106± 0.08
0.5	1.15	0.789	52.5	4.452± 0.36	-0.803± 0.30	-0.934± 0.14
0.5	1.15	0.789	67.5	4.902± 0.33	-0.959± 0.19	-2.627± 0.07
0.5	1.15	0.789	82.5	5.105± 0.34	-0.874± 0.19	-2.557± 0.07
0.5	1.15	0.789	97.5	4.938± 0.35	-0.847± 0.22	-2.934± 0.09
0.5	1.15	0.789	112.5	4.938± 0.34	-0.550± 0.19	-2.478± 0.07
0.5	1.15	0.789	127.5	4.939± 0.83	-1.000± 0.46	-1.852± 0.27
0.5	1.15	0.789	142.5	8.678± 2.20	-3.743± 2.04	0.562± 2.90
0.5	1.17	0.779	7.5	3.713± 0.45	-0.331± 0.24	-1.059± 0.11
0.5	1.17	0.779	22.5	4.173± 0.34	-0.927± 0.19	-0.374± 0.07
0.5	1.17	0.779	37.5	4.817± 0.48	-1.284± 0.31	-0.806± 0.14
0.5	1.17	0.779	52.5	5.701± 0.54	-1.292± 0.41	-1.645± 0.23
0.5	1.17	0.779	67.5	7.084± 0.51	-1.071± 0.20	-3.452± 0.08
0.5	1.17	0.779	82.5	8.029± 0.57	-0.590± 0.48	-3.990± 0.28
0.5	1.17	0.779	97.5	7.002± 0.47	-0.799± 0.25	-4.587± 0.11
0.5	1.17	0.779	112.5	7.352± 0.49	-0.399± 0.25	-3.888± 0.10
0.5	1.17	0.779	127.5	6.752± 0.46	-0.143± 0.20	-3.269± 0.09
0.5	1.17	0.779	142.5	6.396± 1.66	0.979± 1.46	-2.279± 1.50
0.5	1.19	0.768	7.5	4.683± 0.65	-1.122± 0.48	0.560± 0.33
0.5	1.19	0.768	22.5	5.578± 0.84	-0.845± 0.75	0.318± 0.57
0.5	1.19	0.768	37.5	7.227± 0.52	-1.475± 0.26	-1.395± 0.11
0.5	1.19	0.768	52.5	8.185± 0.80	-1.536± 0.63	-3.264± 0.42
0.5	1.19	0.768	67.5	9.722± 0.67	-1.555± 0.45	-5.435± 0.27
0.5	1.19	0.768	82.5	10.126± 0.69	-1.280± 0.28	-6.003± 0.13
0.5	1.19	0.768	97.5	10.496± 0.67	-0.687± 0.21	-6.100± 0.08
0.5	1.19	0.768	112.5	9.976± 0.62	-0.411± 0.18	-5.675± 0.07
0.5	1.19	0.768	127.5	8.936± 0.57	0.187± 0.23	-3.716± 0.10
0.5	1.19	0.768	142.5	7.607± 1.74	1.346± 1.46	-3.774± 1.48
0.5	1.21	0.757	7.5	6.565± 2.60	-1.176± 2.52	-0.567± 3.85
0.5	1.21	0.757	22.5	9.243± 0.75	-0.755± 0.35	-0.731± 0.18
0.5	1.21	0.757	37.5	8.825± 0.65	-1.369± 0.35	-1.456± 0.19
0.5	1.21	0.757	52.5	10.245± 0.83	-1.720± 0.60	-4.074± 0.43
0.5	1.21	0.757	67.5	12.805± 0.98	-0.168± 0.64	-3.635± 0.43
0.5	1.21	0.757	82.5	11.884± 0.80	-1.493± 0.41	-6.450± 0.24
0.5	1.21	0.757	97.5	12.356± 0.76	-0.891± 0.22	-7.339± 0.08
0.5	1.21	0.757	112.5	11.098± 0.68	-0.188± 0.16	-6.412± 0.06
0.5	1.21	0.757	127.5	9.682± 0.63	0.402± 0.20	-4.015± 0.08
0.5	1.21	0.757	142.5	8.937± 1.52	-0.244± 1.27	-2.735± 1.25
0.5	1.23	0.744	22.5	10.699± 0.73	-0.976± 0.23	-0.153± 0.10
0.5	1.23	0.744	37.5	11.451± 0.81	-0.448± 0.36	-1.687± 0.20
0.5	1.23	0.744	52.5	11.645± 0.84	-0.569± 0.47	-2.976± 0.32
0.5	1.23	0.744	67.5	11.503± 0.79	-0.787± 0.48	-4.679± 0.30
0.5	1.23	0.744	82.5	10.452± 0.70	-1.752± 0.39	-6.714± 0.23
0.5	1.23	0.744	97.5	10.658± 0.65	-0.643± 0.19	-6.390± 0.07
0.5	1.23	0.744	112.5	10.021± 0.61	0.194± 0.19	-4.633± 0.07
0.5	1.23	0.744	127.5	8.074± 0.51	0.380± 0.15	-3.657± 0.06
0.5	1.23	0.744	142.5	6.171± 0.98	1.215± 0.88	-4.059± 0.78
0.5	1.25	0.731	22.5	11.692± 0.89	-0.082± 0.27	-0.384± 0.13
0.5	1.25	0.731	37.5	10.812± 0.78	-0.804± 0.41	-1.046± 0.23
0.5	1.25	0.731	52.5	11.382± 0.75	-0.432± 0.35	-2.462± 0.19
0.5	1.25	0.731	67.5	9.824± 0.70	-0.931± 0.45	-3.891± 0.29
0.5	1.25	0.731	82.5	8.885± 0.63	-1.124± 0.42	-4.332± 0.23
0.5	1.25	0.731	97.5	8.154± 0.52	-0.590± 0.22	-4.037± 0.09
0.5	1.25	0.731	112.5	7.026± 0.45	-0.234± 0.13	-2.907± 0.04
0.5	1.25	0.731	127.5	5.463± 0.35	0.137± 0.16	-1.926± 0.05
0.5	1.25	0.731	142.5	4.194± 0.66	0.562± 0.61	-1.339± 0.46
0.5	1.27	0.716	7.5	58.334±16.41	-42.845±15.35	36.013±60.16
0.5	1.27	0.716	22.5	10.910± 0.88	-0.023± 0.29	0.180± 0.14
0.5	1.27	0.716	37.5	11.031± 0.88	-0.219± 0.61	-2.213± 0.41
0.5	1.27	0.716	52.5	9.362± 0.60	-0.173± 0.24	-2.219± 0.11
0.5	1.27	0.716	67.5	7.570± 0.62	-1.195± 0.47	-3.478± 0.27
0.5	1.27	0.716	82.5	7.194± 0.52	-0.679± 0.35	-2.736± 0.18
0.5	1.27	0.716	97.5	5.943± 0.37	-0.512± 0.14	-2.221± 0.05
0.5	1.27	0.716	112.5	4.658± 0.29	-0.038± 0.10	-1.834± 0.03
0.5	1.27	0.716	127.5	3.607± 0.25	0.091± 0.11	-1.316± 0.03
0.5	1.27	0.716	142.5	2.638± 0.72	0.134± 0.63	-1.225± 0.45
0.5	1.29	0.701	7.5	19.215± 2.65	-5.363± 2.79	7.123± 4.57
0.5	1.29	0.701	22.5	10.859± 1.00	0.512± 0.39	-0.954± 0.22
0.5	1.29	0.701	37.5	9.499± 0.88	0.410± 0.61	2.486± 0.44
0.5	1.29	0.701	52.5	7.943± 0.53	-0.499± 0.22	-1.485± 0.09
0.5	1.29	0.701	67.5	6.771± 0.61	-0.630± 0.43	-1.759± 0.24
0.5	1.29	0.701	82.5	5.331± 0.36	-0.922± 0.15	-2.281± 0.05
0.5	1.29	0.701	97.5	4.211± 0.27	-0.603± 0.10	-1.957± 0.03
0.5	1.29	0.701	112.5	3.357± 0.21	-0.292± 0.11	-1.160± 0.03
0.5	1.29	0.701	127.5	2.430± 0.18	-0.092± 0.10	-0.738± 0.03
0.5	1.29	0.701	142.5	1.418± 0.19	0.073± 0.15	-0.573± 0.05
0.5	1.31	0.684	7.5	13.848± 1.19	-0.818± 0.79	-1.479± 0.70
0.5	1.31	0.684	22.5	20.488±10.01	-7.712±10.22	5.929±32.65
0.5	1.31	0.684	37.5	8.609± 0.69	-0.560± 0.58	-2.617± 0.37
0.5	1.31	0.684	52.5	7.231± 0.47	-0.058± 0.20	-1.348± 0.09
0.5	1.31	0.684	67.5	5.527± 0.67	-0.848± 0.62	-2.100± 0.44
0.5	1.31	0.684	82.5	3.971± 0.27	-0.929± 0.15	-1.747± 0.05
0.5	1.31	0.684	97.5	3.398± 0.22	-0.446± 0.11	-1.121± 0.03
0.5	1.31	0.684	112.5	2.337± 0.15	-0.439± 0.10	-0.657± 0.03
0.5	1.31	0.684	127.5	1.724± 0.16	-0.267± 0.10	-0.525± 0.03
0.5	1.31	0.684	142.5	0.917± 0.15	0.079± 0.19	-0.496± 0.07
0.5	1.33	0.667	7.5	11.443± 1.16	1.066± 0.56	0.706± 0.40
0.5	1.33	0.667	22.5	12.483± 2.01	-0.364± 2.26	-0.195± 3.38
0.5	1.33	0.667	37.5	8.152± 0.69	0.523± 0.72	-1.642± 0.52
0.5	1.33	0.667	52.5	6.382± 0.44	0.248± 0.22	-1.649± 0.09
0.5	1.33	0.667	67.5	4.837± 0.49	-0.458± 0.48	-1.746± 0.28
0.5	1.33	0.667	82.5	3.637± 0.24	-0.572± 0.12	-1.864± 0.04
0.5	1.33	0.667	97.5	2.691± 0.17	-0.509± 0.09	-1.353± 0.02
0.5	1.33	0.667	112.5	1.865± 0.13	-0.313± 0.10	-0.793± 0.03
0.5	1.33	0.667	127.5	1.343± 0.11	-0.286± 0.14	-0.588± 0.05
0.5	1.33	0.667	142.5	0.539± 0.33	0.037± 0.31	-0.363± 0.14
0.5	1.35	0.648	7.5	11.045± 0.86	1.222± 0.59	-0.250± 0.39
0.5	1.35	0.648	22.5	6.222± 1.27	4.666± 1.67	-6.508± 2.12
0.5	1.35	0.648	37.5	7.830± 0.74	2.475± 1.08	1.467± 1.00
0.5	1.35	0.648	52.5	5.956± 0.42	0.324± 0.26	-0.830± 0.12
0.5	1.35	0.648	67.5	4.123± 0.31	-0.778± 0.26	-2.022± 0.12
0.5	1.35	0.648	82.5	3.151± 0.21	-0.670± 0.10	-1.665± 0.03
0.5	1.35	0.648	97.5	2.312± 0.16	-0.542± 0.13	-1.326± 0.04
0.5	1.35	0.648	112.5	1.427± 0.10	-0.360± 0.07	-0.323± 0.02
0.5	1.35	0.648	127.5	0.942± 0.08	-0.298± 0.06	-0.308± 0.01
0.5	1.35	0.648	142.5	0.908± 0.28	-0.492± 0.31	0.153± 0.15
0.5	1.37	0.629	7.5	9.668± 0.71	1.076± 0.52	1.288± 0.32
0.5	1.37	0.629	22.5	8.243± 0.75	0.313± 0.92	-0.046± 0.75
0.5	1.37	0.629	37.5	6.765± 0.61	0.294± 0.82	-2.590± 0.65
0.5	1.37	0.629	52.5	5.883± 0.47	0.465± 0.33	-2.107± 0.18
0.5	1.37	0.629	67.5	3.942± 0.34	-0.234± 0.23	-2.457± 0.10
0.5	1.37	0.629	82.5	2.704± 0.18	-0.567± 0.08	-1.429± 0.02
0.5	1.37	0.629	97.5	2.066± 0.14	-0.276± 0.12	-0.577± 0.04
0.5	1.37	0.629	112.5	1.258± 0.11	-0.246± 0.09	-0.580± 0.02
0.5	1.37	0.629	127.5	0.749± 0.07	-0.240± 0.05	-0.213± 0.01
0.5	1.37	0.629	142.5	0.468± 0.07	-0.154± 0.07	0.068± 0.02
0.5	1.39	0.608	7.5	8.515± 0.65	0.529± 0.61	0.570± 0.40
0.5	1.39	0.608	22.5	7.677± 0.62	0.498± 0.43	-0.540± 0.27
0.5	1.39	0.608	37.5	7.727± 2.34	-0.621± 2.31	-0.071± 3.49
0.5	1.39	0.608	52.5	5.364± 0.54	0.939± 0.43	-0.875± 0.26
0.5	1.39	0.608	67.5	3.877± 0.31	-0.056± 0.15	-2.085± 0.05
0.5	1.39	0.608	82.5	2.564± 0.19	-0.439± 0.08	-1.593± 0.02
0.5	1.39	0.608	97.5	1.896± 0.13	-0.477± 0.09	-1.387± 0.02
0.5	1.39	0.608	112.5	1.198± 0.12	-0.256± 0.09	-0.599± 0.02
0.5	1.39	0.608	127.5	0.759± 0.12	-0.202± 0.17	-0.298± 0.06
0.5	1.39	0.608	142.5	0.412± 1.20	-0.118± 1.33	-0.071± 1.53
0.5	1.41	0.586	7.5	7.814± 0.66	0.175± 0.42	0.791± 0.23
0.5	1.41	0.586	22.5	7.093± 0.74	1.108± 0.55	-0.355± 0.37
0.5	1.41	0.586	37.5	7.844± 1.54	-1.257± 1.44	2.432± 1.69
0.5	1.41	0.586	52.5	4.543± 0.33	0.358± 0.31	-2.084± 0.17
0.5	1.41	0.586	67.5	3.854± 0.32	0.378± 0.19	-1.513± 0.08
0.5	1.41	0.586	82.5	2.551± 0.18	-0.254± 0.09	-1.825± 0.02
0.5	1.41	0.586	97.5	1.964± 0.15	-0.395± 0.10	-0.891± 0.03
0.5	1.41	0.586	112.5	1.121± 0.08	-0.168± 0.06	-0.474± 0.01
0.5	1.41	0.586	127.5	0.659± 0.06	-0.099± 0.08	-0.327± 0.02
0.5	1.41	0.586	142.5	0.406± 0.11	-0.078± 0.11	-0.201± 0.03
0.5	1.43	0.562	7.5	7.009± 0.65	-0.609± 0.38	0.415± 0.22
0.5	1.43	0.562	22.5	6.304± 0.81	1.279± 0.91	-0.934± 0.85
0.5	1.43	0.562	37.5	4.752± 1.09	1.322± 0.96	-3.342± 0.91
0.5	1.43	0.562	52.5	4.515± 0.35	0.883± 0.31	-1.512± 0.15
0.5	1.43	0.562	67.5	3.783± 0.30	0.150± 0.12	-2.648± 0.04
0.5	1.43	0.562	82.5	2.678± 0.19	-0.229± 0.11	-1.612± 0.03
0.5	1.43	0.562	97.5	1.747± 0.12	-0.462± 0.10	-1.493± 0.03
0.5	1.43	0.562	112.5	1.294± 0.09	-0.218± 0.06	-0.758± 0.01
0.5	1.43	0.562	127.5	0.833± 0.09	-0.183± 0.06	-0.421± 0.01
0.5	1.43	0.562	142.5	0.576± 0.15	-0.247± 0.18	-0.086± 0.07
0.5	1.45	0.537	7.5	6.186± 0.82	0.257± 0.34	0.880± 0.19
0.5	1.45	0.537	22.5	5.961± 0.71	1.035± 0.75	-1.717± 0.58
0.5	1.45	0.537	37.5	5.339± 0.63	0.664± 0.52	-2.502± 0.35
0.5	1.45	0.537	52.5	4.806± 0.40	0.664± 0.36	-3.082± 0.20
0.5	1.45	0.537	67.5	3.767± 0.25	0.052± 0.10	-2.405± 0.03
0.5	1.45	0.537	82.5	3.055± 0.20	-0.228± 0.15	-2.274± 0.05
0.5	1.45	0.537	97.5	2.198± 0.16	-0.382± 0.09	-1.636± 0.03
0.5	1.45	0.537	112.5	1.501± 0.11	-0.230± 0.08	-0.766± 0.02
0.5	1.45	0.537	127.5	1.041± 0.09	-0.290± 0.05	-0.415± 0.01
0.5	1.45	0.537	142.5	0.525± 0.10	-0.074± 0.13	-0.438± 0.04
0.5	1.47	0.511	7.5	6.493± 0.51	1.240± 0.44	0.757± 0.27
0.5	1.47	0.511	22.5	5.419± 0.64	0.281± 0.59	-2.034± 0.41
0.5	1.47	0.511	37.5	5.346± 0.52	1.388± 0.41	-2.538± 0.26
0.5	1.47	0.511	52.5	4.663± 0.46	0.623± 0.45	-3.479± 0.26
0.5	1.47	0.511	67.5	4.404± 0.39	0.171± 0.09	-2.818± 0.02
0.5	1.47	0.511	82.5	3.475± 0.24	-0.421± 0.13	-2.452± 0.04
0.5	1.47	0.511	97.5	2.723± 0.19	-0.429± 0.14	-2.035± 0.04
0.5	1.47	0.511	112.5	2.011± 0.16	-0.440± 0.07	-1.093± 0.02
0.5	1.47	0.511	127.5	1.403± 0.11	-0.249± 0.08	-0.911± 0.02
0.5	1.47	0.511	142.5	1.097± 0.24	-0.283± 0.29	-0.724± 0.13
0.5	1.49	0.484	7.5	6.737± 0.79	1.502± 0.61	-1.058± 0.40
0.5	1.49	0.484	22.5	5.545± 1.30	1.010± 1.66	-2.434± 2.12
0.5	1.49	0.484	37.5	5.534± 0.55	1.060± 0.57	-0.767± 0.40
0.5	1.49	0.484	52.5	4.024± 1.12	1.384± 1.05	-5.446± 1.05
0.5	1.49	0.484	67.5	4.338± 0.33	0.059± 0.18	-2.964± 0.06
0.5	1.49	0.484	82.5	3.849± 0.28	-0.205± 0.15	-2.743± 0.06
0.5	1.49	0.484	97.5	3.217± 0.24	-0.474± 0.19	-2.787± 0.07
0.5	1.49	0.484	112.5	2.829± 0.22	-0.466± 0.18	-2.051± 0.06
0.5	1.49	0.484	127.5	2.097± 0.18	-0.582± 0.15	-1.631± 0.05
0.5	1.49	0.484	142.5	1.543± 0.30	-0.569± 0.31	-0.823± 0.14
0.5	1.51	0.455	37.5	3.093± 1.47	-1.948± 2.77	-7.737± 4.61
0.5	1.51	0.455	52.5	1.924± 1.92	2.315± 2.22	-8.786± 3.16
0.5	1.51	0.455	67.5	2.791± 0.32	0.089± 0.15	-1.844± 0.05
0.5	1.51	0.455	82.5	2.629± 0.57	-0.143± 0.69	-2.840± 0.50

Q^2	W	ϵ	θ	$\sigma_T + \epsilon\sigma_L$	σ_{TL}	σ_{TT}
0.5	1.51	0.455	97.5	2.471± 0.37	-0.746± 0.25	-3.246± 0.10
0.5	1.51	0.455	112.5	2.252± 0.25	-0.437± 0.27	-2.160± 0.12
0.5	1.51	0.455	127.5	2.035± 1.03	-0.420± 1.35	-1.524± 1.54
0.6	1.11	0.763	22.5	1.694± 0.28	-0.258± 0.18	0.546± 0.07
0.6	1.11	0.763	37.5	2.421± 0.26	-0.516± 0.14	-0.484± 0.05
0.6	1.11	0.763	52.5	2.101± 0.50	-0.513± 0.41	-0.604± 0.24
0.6	1.11	0.763	67.5	2.196± 0.26	-0.558± 0.28	-0.288± 0.13
0.6	1.11	0.763	82.5	1.964± 0.20	-0.301± 0.20	-1.035± 0.08
0.6	1.11	0.763	97.5	1.823± 0.40	-0.664± 0.28	-1.277± 0.13
0.6	1.11	0.763	112.5	1.580± 0.72	-0.614± 0.70	-1.297± 0.55
0.6	1.13	0.752	22.5	2.781± 0.28	-0.057± 0.21	0.329± 0.09
0.6	1.13	0.752	37.5	2.911± 0.30	-0.573± 0.16	-0.596± 0.06
0.6	1.13	0.752	52.5	2.941± 0.35	-0.387± 0.31	-0.073± 0.17
0.6	1.13	0.752	67.5	2.824± 0.26	-0.673± 0.22	-1.128± 0.09
0.6	1.13	0.752	82.5	2.995± 0.23	-0.586± 0.12	-1.557± 0.04
0.6	1.13	0.752	97.5	2.847± 0.25	-0.502± 0.20	-1.417± 0.08
0.6	1.13	0.752	112.5	2.649± 0.33	-0.377± 0.31	-1.562± 0.16
0.6	1.13	0.752	127.5	2.866± 0.44	-0.650± 0.41	-1.025± 0.22
0.6	1.15	0.742	22.5	3.629± 0.36	-0.644± 0.21	-1.393± 0.08
0.6	1.15	0.742	37.5	3.167± 0.42	-0.912± 0.43	-1.821± 0.24
0.6	1.15	0.742	52.5	3.272± 0.70	-1.202± 0.75	-2.286± 0.61
0.6	1.15	0.742	67.5	4.034± 0.29	-1.075± 0.18	-1.943± 0.07
0.6	1.15	0.742	82.5	4.300± 0.35	-0.364± 0.19	-1.633± 0.08
0.6	1.15	0.742	97.5	4.509± 0.35	-0.374± 0.26	-2.661± 0.13
0.6	1.15	0.742	112.5	3.906± 0.30	-0.564± 0.17	-2.547± 0.06
0.6	1.15	0.742	127.5	3.787± 0.41	-0.392± 0.22	-1.837± 0.10
0.6	1.15	0.742	142.5	6.362± 1.91	-2.414± 1.88	0.906± 2.56
0.6	1.17	0.730	22.5	3.899± 0.79	-0.238± 0.80	0.531± 0.68
0.6	1.17	0.730	37.5	3.840± 0.39	-1.192± 0.29	-1.054± 0.14
0.6	1.17	0.730	52.5	5.724± 1.05	-0.484± 1.20	-1.972± 1.11
0.6	1.17	0.730	67.5	5.386± 0.41	-1.455± 0.26	-3.852± 0.11
0.6	1.17	0.730	82.5	6.273± 0.45	-0.903± 0.29	-4.025± 0.13
0.6	1.17	0.730	97.5	5.997± 0.43	-0.646± 0.22	-3.741± 0.10
0.6	1.17	0.730	112.5	5.815± 0.38	0.137± 0.20	-3.315± 0.07
0.6	1.17	0.730	127.5	5.594± 0.41	-0.267± 0.32	-2.349± 0.15
0.6	1.17	0.730	142.5	6.416± 1.76	0.529± 1.77	-2.563± 2.35
0.6	1.19	0.718	22.5	4.580± 0.57	-0.849± 0.34	-1.383± 0.17
0.6	1.19	0.718	37.5	5.755± 0.58	-0.906± 0.45	-0.376± 0.27
0.6	1.19	0.718	52.5	6.580± 0.69	-1.566± 0.63	-2.904± 0.48
0.6	1.19	0.718	67.5	8.403± 0.68	-0.575± 0.56	-3.656± 0.41
0.6	1.19	0.718	82.5	8.310± 0.56	-1.020± 0.30	-5.952± 0.16
0.6	1.19	0.718	97.5	8.933± 0.61	-0.469± 0.26	-5.504± 0.12
0.6	1.19	0.718	112.5	8.264± 0.54	0.035± 0.22	-4.498± 0.09
0.6	1.19	0.718	127.5	7.675± 0.56	0.218± 0.31	-3.107± 0.15
0.6	1.19	0.718	142.5	6.351± 0.89	0.863± 0.85	-2.880± 0.74
0.6	1.21	0.704	22.5	7.259± 0.80	-1.361± 0.37	-0.350± 0.19
0.6	1.21	0.704	37.5	7.749± 0.63	-0.722± 0.42	-0.771± 0.24
0.6	1.21	0.704	52.5	8.603± 0.71	-1.635± 0.48	-4.757± 0.30
0.6	1.21	0.704	67.5	9.952± 0.73	-1.279± 0.52	-4.917± 0.35
0.6	1.21	0.704	82.5	10.180± 0.72	-0.913± 0.47	-5.997± 0.30
0.6	1.21	0.704	97.5	10.446± 0.66	-0.542± 0.24	-5.591± 0.11
0.6	1.21	0.704	112.5	9.808± 0.66	0.339± 0.41	-5.239± 0.23
0.6	1.21	0.704	127.5	8.760± 0.59	0.590± 0.23	-4.167± 0.10
0.6	1.21	0.704	142.5	6.591± 1.37	0.957± 1.34	-3.864± 1.38
0.6	1.23	0.690	22.5	8.618± 0.84	-0.649± 0.38	-0.232± 0.21
0.6	1.23	0.690	37.5	9.234± 0.70	-0.931± 0.38	-0.557± 0.23
0.6	1.23	0.690	52.5	10.844± 0.82	0.302± 0.62	-1.578± 0.42
0.6	1.23	0.690	67.5	9.592± 0.79	-2.084± 0.61	-6.395± 0.44
0.6	1.23	0.690	82.5	8.972± 0.71	-1.632± 0.56	-5.479± 0.37
0.6	1.23	0.690	97.5	8.957± 0.55	-0.806± 0.22	-4.975± 0.09
0.6	1.23	0.690	112.5	8.148± 0.53	0.305± 0.20	-4.716± 0.09
0.6	1.23	0.690	127.5	7.130± 0.46	0.606± 0.20	-3.026± 0.08
0.6	1.23	0.690	142.5	7.504± 1.05	-1.681± 1.04	0.629± 0.99
0.6	1.25	0.675	22.5	8.725± 0.98	0.322± 0.41	3.193± 0.25
0.6	1.25	0.675	37.5	10.228± 0.85	0.569± 0.51	-1.810± 0.33
0.6	1.25	0.675	52.5	9.522± 0.68	0.043± 0.39	-1.583± 0.23
0.6	1.25	0.675	67.5	8.376± 0.59	-0.634± 0.38	-1.673± 0.22
0.6	1.25	0.675	82.5	7.083± 0.58	-1.476± 0.50	-5.152± 0.32
0.6	1.25	0.675	97.5	6.816± 0.43	-0.535± 0.16	-3.295± 0.06
0.6	1.25	0.675	112.5	5.785± 0.37	-0.205± 0.25	-2.848± 0.11
0.6	1.25	0.675	127.5	4.852± 0.34	-0.047± 0.16	-1.667± 0.06
0.6	1.25	0.675	142.5	3.961± 0.50	0.091± 0.50	-0.632± 0.34
0.6	1.27	0.660	7.5	6.519± 3.15	6.526± 3.60	-5.081± 6.56
0.6	1.27	0.660	22.5	12.116± 1.68	0.158± 0.59	-5.376± 0.40
0.6	1.27	0.660	37.5	9.482± 0.79	-0.165± 0.47	-1.871± 0.32
0.6	1.27	0.660	52.5	8.546± 0.65	0.310± 0.37	-0.868± 0.20
0.6	1.27	0.660	67.5	7.293± 0.68	-0.216± 0.61	-1.224± 0.45
0.6	1.27	0.660	82.5	5.670± 0.46	-1.023± 0.34	-2.716± 0.18
0.6	1.27	0.660	97.5	4.810± 0.36	-1.039± 0.34	-2.696± 0.18
0.6	1.27	0.660	112.5	4.218± 0.29	-0.279± 0.20	-2.096± 0.08
0.6	1.27	0.660	127.5	3.083± 0.25	0.104± 0.14	-0.906± 0.05
0.6	1.27	0.660	142.5	2.144± 0.30	0.038± 0.28	-0.899± 0.13
0.6	1.29	0.643	7.5	10.927± 1.19	-1.076± 1.00	2.494± 0.98
0.6	1.29	0.643	22.5	32.875±16.21	-22.147±16.45	14.492±66.68
0.6	1.29	0.643	37.5	9.613± 1.21	0.795± 1.29	-1.005± 1.36
0.6	1.29	0.643	52.5	7.230± 0.55	-0.272± 0.31	-1.807± 0.16
0.6	1.29	0.643	67.5	5.405± 0.44	-1.205± 0.38	-1.620± 0.22
0.6	1.29	0.643	82.5	4.833± 0.35	-0.551± 0.23	-1.671± 0.10
0.6	1.29	0.643	97.5	3.725± 0.26	-0.528± 0.20	-1.717± 0.07
0.6	1.29	0.643	112.5	2.816± 0.20	-0.286± 0.09	-1.443± 0.03
0.6	1.29	0.643	127.5	1.822± 0.18	-0.109± 0.11	-0.541± 0.03
0.6	1.29	0.643	142.5	1.400± 0.75	0.187± 0.76	-1.164± 0.60
0.6	1.31	0.625	7.5	8.989± 0.98	0.774± 0.81	1.616± 0.71
0.6	1.31	0.625	22.5	11.234± 3.78	0.305± 4.86	-1.951± 9.44
0.6	1.31	0.625	37.5	8.146± 0.71	0.232± 0.72	-0.283± 0.52
0.6	1.31	0.625	52.5	6.344± 0.48	-0.197± 0.36	-0.865± 0.18
0.6	1.31	0.625	67.5	5.185± 0.42	-0.267± 0.33	-1.387± 0.17
0.6	1.31	0.625	82.5	3.999± 0.31	-0.567± 0.17	-1.620± 0.07
0.6	1.31	0.625	97.5	2.869± 0.23	-0.588± 0.19	-1.406± 0.07
0.6	1.31	0.625	112.5	2.156± 0.16	-0.310± 0.12	-0.579± 0.04
0.6	1.31	0.625	127.5	1.378± 0.11	-0.151± 0.09	-0.642± 0.02
0.6	1.31	0.625	142.5	0.796± 0.23	0.085± 0.15	-0.422± 0.05
0.6	1.33	0.606	7.5	10.663± 1.18	0.960± 0.81	1.251± 0.65
0.6	1.33	0.606	22.5	8.178± 1.86	0.488± 2.25	-0.263± 3.35
0.6	1.33	0.606	37.5	7.542± 0.69	-0.130± 0.55	-2.202± 0.39
0.6	1.33	0.606	52.5	5.987± 0.46	0.161± 0.35	-0.516± 0.18
0.6	1.33	0.606	67.5	4.482± 0.41	-0.435± 0.35	-1.028± 0.18
0.6	1.33	0.606	82.5	3.344± 0.25	-0.489± 0.15	-0.827± 0.06
0.6	1.33	0.606	97.5	2.464± 0.20	-0.617± 0.16	-0.491± 0.05
0.6	1.33	0.606	112.5	1.637± 0.27	-0.348± 0.16	-0.764± 0.06
0.6	1.33	0.606	127.5	1.076± 0.10	-0.049± 0.09	-0.297± 0.02
0.6	1.33	0.606	142.5	0.596± 0.41	-0.190± 0.55	-0.184± 0.39
0.6	1.35	0.585	7.5	10.280± 0.95	-1.230± 1.02	2.510± 0.88
0.6	1.35	0.585	22.5	8.556± 1.06	0.161± 0.83	-0.323± 0.66
0.6	1.35	0.585	52.5	5.469± 0.47	0.143± 0.41	-1.736± 0.23
0.6	1.35	0.585	67.5	4.306± 0.47	-0.125± 0.54	-1.657± 0.34
0.6	1.35	0.585	82.5	2.913± 0.21	-0.686± 0.14	-1.253± 0.04
0.6	1.35	0.585	97.5	2.072± 0.16	-0.632± 0.14	-1.029± 0.04
0.6	1.35	0.585	112.5	1.391± 0.12	-0.351± 0.10	-0.478± 0.03
0.6	1.35	0.585	127.5	0.899± 0.11	-0.148± 0.16	-0.184± 0.06
0.6	1.35	0.585	142.5	0.470± 0.10	-0.178± 0.12	0.027± 0.03
0.6	1.37	0.564	7.5	7.837± 0.88	-0.683± 0.81	0.858± 0.64
0.6	1.37	0.564	22.5	7.909± 0.82	0.474± 0.63	-2.110± 0.48
0.6	1.37	0.564	37.5	9.252± 2.69	-3.438± 2.74	2.210± 4.48
0.6	1.37	0.564	52.5	5.254± 0.42	0.213± 0.47	-1.140± 0.28
0.6	1.37	0.564	67.5	3.807± 0.35	0.000± 0.29	-1.035± 0.14
0.6	1.37	0.564	82.5	2.637± 0.20	-0.346± 0.18	-1.339± 0.07
0.6	1.37	0.564	97.5	1.979± 0.18	-0.177± 0.16	0.033± 0.06
0.6	1.37	0.564	112.5	1.076± 0.10	-0.263± 0.10	-0.284± 0.03
0.6	1.37	0.564	127.5	0.667± 0.10	-0.255± 0.07	-0.205± 0.02
0.6	1.37	0.564	142.5	0.454± 0.14	-0.144± 0.19	-0.152± 0.07
0.6	1.39	0.541	7.5	7.566± 1.79	0.416± 0.65	0.104± 0.47
0.6	1.39	0.541	22.5	6.792± 0.70	0.685± 0.72	-1.268± 0.56
0.6	1.39	0.541	37.5	8.205± 2.06	-0.844± 2.04	4.278± 2.71
0.6	1.39	0.541	52.5	4.322± 0.44	-0.049± 0.51	-2.415± 0.34
0.6	1.39	0.541	67.5	3.496± 0.47	0.028± 0.47	-1.563± 0.27
0.6	1.39	0.541	82.5	2.549± 0.21	-0.058± 0.17	-0.935± 0.06
0.6	1.39	0.541	97.5	1.713± 0.20	-0.382± 0.15	-0.896± 0.05
0.6	1.39	0.541	112.5	1.138± 0.20	-0.284± 0.18	-0.297± 0.06
0.6	1.39	0.541	127.5	0.542± 0.09	-0.130± 0.11	-0.097± 0.03
0.6	1.39	0.541	142.5	0.419± 0.10	-0.184± 0.11	0.178± 0.04
0.6	1.41	0.518	67.5	2.856± 0.47	-0.527± 0.44	0.574± 0.26
0.6	1.41	0.518	82.5	2.367± 0.45	0.044± 0.46	-0.610± 0.30
0.6	1.41	0.518	97.5	1.817± 0.56	-0.631± 0.54	-2.507± 0.33